

Electro-Optic Characterization of Thin-Film Electroluminescent Devices

B. A. Baukol, P. D. Keir, B. A. Cleary, C. A. Nevers, C. M. Maddix, T. K. Plant, and J. F.

Wager

Department of Electrical and Computer Engineering

Oregon State University

Corvallis, OR 97331-3211

Corresponding Author:

John F. Wager

Department of Electrical and Computer Engineering

Oregon State University

Corvallis, OR 97331-3211

jfw@ece.orst.edu

Phone: (541) 737-2994

Fax: (541) 737-1300

Contents

1	INTRODUCTION	5
2	SURVEY OF PREVIOUS WORK	6
2.1	Transient Luminance [L(t)] Experiments	7
2.2	Photo-Depolarization (PDP) Experiments	12
3	STANDARD ELECTRO-OPTIC CHARACTERIZATION	14
3.1	Luminance-Voltage Characterization	14
3.2	Efficiency-Voltage Characterization	17
3.3	CIE Color Coordinates	19
4	NON-STANDARD ELECTRO-OPTIC CHARACTERIZATION	21
4.1	Photo-Induced Charge and Luminescence Measurements	21
4.1.1	Evaporated ZnS:Mn ACTFEL Device PIQ/PIL Results	23
4.1.2	SrS ACTFEL Device PIQ/PIL Results	25
4.2	Subthreshold Voltage-Induced Transferred Charge Analysis	28
4.2.1	ZnS:Mn ACTFEL Device VIQ Results	29
4.2.2	SrS: ACTFEL Device VIQ Results	32
4.2.3	Lanthanide Doping Studies	33

Abstract

Methods for accomplishing electro-optic (EO) characterization of alternating-current thin-film electroluminescent (ACTFEL) display devices are reviewed. The three most important ACTFEL device EO measurements involve assessment of the luminance, luminance efficiency, and color of the display via luminance-voltage, efficiency-voltage, and CIE color coordinate measurements, respectively. These EO techniques provide essential information that determines the viability of an ACTFEL phosphor for commercial display applications. The fundamental objective of all other ACTFEL device EO measurements is to provide insight into the materials properties, device physics operation, and/or aging properties/mechanisms of a given ACTFEL phosphor or device. Such ACTFEL device EO assessment methods which are reviewed herein include transient luminance, photo-depolarization, photoinduced transferred charge, photoinduced luminescence, subthreshold voltage-induced transferred charge, and lanthanide doping studies.

1 INTRODUCTION

An alternating-current thin-film electroluminescent (ACTFEL) device is an electro-optic device in which electrical energy (in the form of some type of AC voltage waveform) is applied as an input, and visible light constitutes the desired output. Thus, an ACTFEL device functions as a display. ACTFEL devices comprise a small, niche flat-panel display market. They are now used in commercial monochrome and multicolor flat-panel displays. [1] Also, they are under development for full-color display, miniature display, hard-copy, and other light source applications. Advantages of ACTFEL displays include long-lifetime, broad operating temperature, ruggedness, and wide viewing angle. ACTFEL displays are an appropriate choice for a variety of military, automotive, industrial, and medical applications in which the best attributes of ACTFEL technology are highly valued.

An ACTFEL device is a thin-film stack. It typically consists of a phosphor layer doped with a luminescent impurity (e.g. ZnS:Mn, SrS:Cu, etc.) which is sandwiched between two insulators which are in turn contacted by an opaque and a transparent electrode. Usually an ACTFEL stack is deposited onto a glass substrate with the transparent conductor as the bottom electrode so that light is viewed through the substrate glass. However, inverted structures are sometimes used, in which case the electrodes are reversed and light is viewed from the top side of the device.

Six primary physical processes are responsible for ideal ACTFEL device operation, as illustrated in Fig. 1. First, when a large enough voltage is applied to the ACTFEL device, electrons are tunnel-emitted into the phosphor conduction band. Second, electrons injected into the phosphor conduction band gain energy from the electric field and are transported across the phosphor. Third, as hot electrons transit the phosphor, a fraction of them excite luminescent impurities from their ground state (G) to their excited state (E). Fourth, relaxation of the electron from its excited state back to its ground state results in photon emission. Fifth, transported electrons reach

the phosphor/insulator interface where they are trapped. Sixth, photons generated via radiative recombination of luminescent impurities out-couple from the ACTFEL stack and are observed by the viewer. Note that the device physics operation of real ACTFEL devices is normally more complicated than in the ideal picture just described. [2, 3]

The purpose of this article is to review electro-optic (EO) characterization studies and methods that have been used to assess ACTFEL devices. This review is divided into three primary sections involving: (i) a survey of selected previous work, (ii) a discussion of the three most common EO characterization techniques employed, and (iii) a description of three non-standard EO characterization methods that we have found particularly useful for ACTFEL device physics and aging assessment. The interested reader may find the following references of interest for obtaining a broad introduction to ACTFEL device physics, characterization, and modeling. [1, 2, 3, 4, 5, 6, 7, 8, 9, 10, 11] Note that since EO characterization is the focus of this article, optical assessment methods such as optical absorption, reflectivity, or transmission measurements, [8, 12] photoluminescence, [8, 12] photoluminescence excitation, [8] photoluminescence decay, [8, 12] cathodoluminescence, [8, 12] photoconductivity, [13, 14] photocapacitance, [15, 16] and thermally stimulated luminescence [17, 18, 19, 20] are not considered herein.

2 SURVEY OF PREVIOUS WORK

Electro-optic (EO) characterization of ACTFEL devices gives vital information about the optical performance of these displays not available through purely electrical measurement techniques. The three most important ACTFEL device EO measurements involve assessment of the luminance, luminance efficiency, and color of the display via luminance-voltage [L-V], efficiency-voltage [η -V], and CIE color coordinate measurements, respectively. These EO techniques provide essential information that establishes the viability of an ACTFEL phosphor for commercial display applica-

tions. Given the fundamental importance of these EO measurements, they are discussed in detail in Section 3 of this review.

The fundamental objective of all other ACTFEL device EO measurements is to provide insight into the materials properties, device physics operation, and/or aging properties/mechanisms of a given ACTFEL phosphor or device. Such non-standard ACTFEL assessment methods that we have found particularly useful for device physics/aging studies include photoinduced transferred charge [PQ or PIQ], photoinduced luminescence [PIL], subthreshold voltage-induced transferred charge [VIQ], and lanthanide doping studies, all of which are discussed in detail in Section 4 of this review. Two other EO measurements, transient luminance [$L(t)$] and photo-depolarization [PDP] measurements are briefly reviewed in Section 2.1.

Finally, numerous other ACTFEL device EO measurements have been reported in the literature. [16, 21, 22, 23, 24, 25, 26, 27, 28, 29, 30, 31, 32, 33, 34, 35] Typically, these EO measurements involve some type of irradiation and monitoring of a given transient or steady-state property of the ACTFEL device. Although these measurements do not lend themselves to a detailed exposition in this review, they are cited as possible sources of inspiration for future research.

2.1 Transient Luminance [$L(t)$] Experiments

One of the earliest applications of transient luminance [$L(t)$] analysis was accomplished by Tanaka et al. who compared time-resolved photoluminescence to electroluminescence in ZnS:Mn ACTFEL devices. [36] In photoluminescence, they observed a time delay in the Mn emission due to energy transfer from the ZnS host to the Mn luminescent impurities. However, almost no time delay was observed in electroluminescence. Thus, they interpreted this result as experimental evidence for hot electron impact excitation of Mn luminescent impurities as the physical mechanism responsible for electroluminescence in ZnS:Mn ACTFEL devices.

Spectrally-resolved $L(t)$ measurements of ZnS:Mn ACTFEL devices reveal that in addition to Mn-related electroluminescence, a fast-decaying, broad-band emission is invariably present. [13, 14, 37, 38, 39, 40] This broad band emission is sometimes referred to as 'hot electron luminescence' to denote its origin as radiative recombination of heated electrons transiting the phosphor. Monitoring the blue portion of this $L(t)$ emission, to avoid the longer wavelength Mn emission, is an effective optical probe for discerning conduction current trends during ACTFEL operation since this 'blue emission' transient correlates very well with the conduction current transient. [39] An advantage of this optical conduction current probe is that there is no displacement current effect to complicate transient conduction current estimation.

Early ACTFEL researchers recognized that assessment of this 'hot electron luminescence' could provide some information regarding the kinetic energy distribution of the electrons transiting the phosphor. [13, 37] For evaporated ZnS:Mn ACTFEL devices, Douglas et al. found this hot electron luminescence spectrum to be broad and essentially featureless up to a high energy cut-off of approximately 3.7 eV, which is determined by optical absorption of photons across the bandgap of ZnS. [40] If the hot electron luminescence spectrum is interpreted as arising from radiative recombination of electrons exclusively within the conduction band, [41] then this result could be construed as evidence that a significant fraction of the hot electrons have kinetic energies in excess of that required for the excitation of blue electroluminescence in ZnS (i.e. ~ 2.6 eV). However, this conclusion is inconsistent with lanthanide doping experiments, as presented in Section 4.2.3, which assert that electrons in ZnS are inadequately heated for blue electroluminescence. This inconsistency between hot electron luminescence and lanthanide doping experiments can be resolved by recognizing that the hot electron luminescence spectrum arises from the radiative deexcitation of both electrons within the conduction band and of electrons with ionized traps within the phosphor bandgap. [42] Thus, in general, the energy of an electron giving rise to hot electron luminescence

is partially kinetic energy of motion and partially potential energy associated with the energy of separation between the bottom of the conduction band and the trap into which the electron recombines. Recognizing this, it is clear that the kinetic energy distribution of hot electrons transiting the phosphor cannot be unambiguously deduced from hot electron luminescence experiments since the radiative energy associated with hot electron luminescence can be either potential or kinetic in origin. Given this, we prefer lanthanide doping experiments for estimation of the high energy tail of the hot electron distribution.

L(t) analysis is often used to deduce whether dynamic positive space charge is present in a phosphor during ACTFEL operation. The L(t) characteristic signature of dynamic space charge is the existence of trailing edge emission (TEE) at the end of an applied voltage pulse. [43, 44, 45, 46, 47, 48, 49, 50, 51, 52] Although TEE is observed for applied voltage waveforms other than conventional bipolar pulses, [46, 47, 48, 51] the following discussion exclusively focuses on bipolar pulses.

The idea of TEE is as follows. During an applied voltage pulse, electrons transit the phosphor from the cathode to the anode phosphor/insulator interface. This charge transfer leads to an accumulation of negative charge near the anode interface and positive charge near the cathode interface, and a concomitant counter (polarization) electric field in the phosphor which opposes the electric field associated with the applied voltage pulse. At the end of the applied voltage pulse, when the voltage is ramping down to zero, the total phosphor electric field, which arises from both the applied voltage and polarization charge, decreases in magnitude and subsequently reverse its polarity. It is possible that once the electric field at the anode interface reverses its polarity, some of the accumulated electrons which constitute the polarization charge could be 'back-injected' into the phosphor if these electrons are in shallow enough energy states and/or the phosphor polarization electric field is sufficiently large to allow for electron injection. In principle, a sufficiently large

transfer of interfacial charge across the phosphor could give rise to a large enough polarization field for back-injection and impact excitation of luminescent impurities, giving rise to TEE. Such an interfacial charge mediated TEE process is unlikely, although it has been witnessed in thick dielectric ZnS:Mn EL devices at large over-voltages (greater than ~ 65 V). [52]

A more common TEE scenario involves the presence of positive space charge in the phosphor, which results in a nonuniform bending of the energy bands. In such a situation, the anode field during the applied voltage pulse is quite small, so that it reverses polarity as the applied voltage amplitude ramps back to zero. In fact, when a large amount of positive space charge is present, TEE is observed as soon as the amplitude of the applied voltage pulse begins to decrease. This zero-delay TEE emission is attributed to radiative recombination of back-injected electrons; radiative recombination can occur as a consequence of electrons recombining with ionized luminescent impurities or via a process involving electron recombination with ionized traps and subsequent energy transfer to the luminescent impurity. Note that back-injection/impact excitation is an improbable mechanism for zero-delay TEE since it is unlikely that the anode electric field would be high enough for impact excitation to occur at zero-delay. Rather, when TEE arises from back-injection/impact excitation, a delayed TEE signal is more probable; this delayed TEE signal often occurs precisely at the end of the applied voltage pulse, when the polarization field is reversed in polarity and is at its maximum post-pulse amplitude.

TEE is omnipresent in SrS:Ce and most alkaline earth sulfide phosphor ACTFEL devices. In such devices, the TEE emission peak is sometimes larger than the leading edge emission peak. Note that positive space charge plays dual roles in a SrS:Ce TEE process; first, it bends the energy bands so that electron back-injection can occur and second, it acts as the radiative recombination site. Since TEE is so pervasive in SrS:Ce ACTFEL devices, it is evident that the impact ionization/radiative recombination electroluminescence mechanism plays an important role in the operation of

such devices. Whether or not Ce impact excitation is an important electroluminescence mechanism in SrS is less clear.

Typically, TEE is not observed in ZnS:Mn ACTFEL devices. [52] However for certain types of ZnS:Mn ACTFEL devices, e.g., those grown by atomic layer epitaxy (ALE) using a chlorine-containing precursor gas, a weak TEE is observed. [40, 43] This peculiar TEE is most likely due to space charge associated with self-compensation-induced Cl_S-V_{Zn} defect complexes for the case of ALE(Cl) ZnS:Mn (this identification arises from the presence of blue TEE, which is ascribed to self-activated donor-acceptor emission [40]). TEE in ZnS:Mn is usually attributed to the back-injection of electrons from anode interface states and impact excitation of Mn in the high field region near the anode when the applied voltage is removed. [47, 48] Note that for this type of TEE, the role of positive space charge is to bend the energy bands so that electron back-injection/impact excitation can occur.

In summary, zero-delay TEE is strong evidence for the presence of positive space charge in the phosphor and an electroluminescence mechanism involving impact ionization/radiative recombination. Delayed TEE most likely arises from positive space charge, although it can also be observed under non-standard operating conditions in which the interface-related polarization field is anomalously large. Moreover, delayed TEE can involve either impact excitation or impact ionization/radiative recombination electroluminescence mechanisms.

Electroluminescent decay measurements are a variant of $L(t)$ analysis in which a very short ($\sim 1-3 \mu\text{sec}$) voltage pulse is used to excite the ACTFEL device and the decay portion of the $L(t)$ curve is monitored and assessed. [5, 13, 53, 54, 55] An ideal decay curve would exhibit a simple, exponential decay with time, characterized by a single time constant related to the radiative lifetime of the luminescent impurity; a longer lifetime corresponds to a more perfect crystal environment and fewer nonradiative decay pathways.

However, most electroluminescent decay curves do not decay in a simple, exponential manner. Nonexponential electroluminescence decay may be a consequence of multiple exponential radiative or nonradiative decay mechanisms being operative or may be due to the fact that radiative recombination behaves according to nonlinear kinetics, due to interactions between luminescent impurities, for example. [5] Thus, although electroluminescence decay curves can be obtained in a relatively straightforward fashion, a detailed interpretation of these curves is not always clear-cut.

Excitation/deexcitation yield experiments constitute another variant of conventional $L(t)$ analysis. [5, 56, 57, 58] These experiments consist of applying a very short ($\sim 1-3 \mu\text{sec}$) voltage pulse to the ACTFEL device and monitoring the transferred charge and transient luminance arising from this voltage pulse. From this measurement, the excitation yield (i.e. the ratio of the number of excited luminescent impurities to the number of electrons transiting the phosphor) can be estimated as a product of the peak luminance and the radiative decay time divided by the transferred charge. Also, the deexcitation yield is estimated as the total integrated luminance induced by the voltage pulse divided by a product of the peak luminance and the radiative decay time. Thus, the goal of these experiments is to provide insight into the nature of hot electron transport in an ACTFEL phosphor. Excitation/deexcitation yield experiments of ALE ZnS:Mn ACTFEL devices reveal that both of these yields (i) are asymmetric with respect to the applied voltage pulse polarity and (ii) tend to decrease with increasing applied voltage as the threshold is approached, but to be relatively constant for voltages both above and below the threshold voltage. These trends appear to be associated with the presence of space charge within the phosphor.

2.2 Photo-Depolarization (PDP) Experiments

Photo-depolarization (PDP) experiments, as pioneered by Vlasenko and co-workers, [59, 60, 61, 62] appear to be well-suited to ACTFEL aging assessment. PDP experiments are accomplished by

first applying a below-threshold DC voltage to the ACTFEL device and then stimulating the ACTFEL device with a variable wavelength light source. As the ACTFEL device is illuminated, an excitation-induced, wavelength-dependent photo-current is measured. The polarity of the applied DC voltage is then reversed and the device is photo-depolarized (i.e. optically reset). Following PDP measurements with both polarities, the ACTFEL device is aged for a period of time. PDP experiments are then performed on the aged sample and this data is used to determine the aging properties of the ACTFEL device.

Vlasenko and co-workers have performed PDP measurements on ZnS:Mn ACTFEL devices whose phosphor layers were deposited by thermal evaporation, atomic layer epitaxy using chlorine as a constituent of the precursor gas [ALE (Cl)], and atomic layer epitaxy with diethyl zinc as a precursor gas [ALE (DEZ)]. [59, 60, 61] The PDP experiments of evaporated ZnS:Mn ACTFEL devices are interpreted as showing a decrease in the concentration of both acceptor and donor-like traps within the phosphor as a function of aging. This decrease in concentration is attributed to gettering of defects to grain boundaries. PDP experiments on ALE (Cl) ZnS:Mn ACTFEL devices are interpreted as showing that the aging process is due to migration of Cl, resulting in a shallower source of free electrons; i.e. the Cl atoms diffuse and sit on S sites, becoming shallow donors as aging progresses. In contrast, ALE (DEZ) ACTFEL devices exhibit a reversal of the PDP polarity with aging, which they attribute to the depletion of electrons at the phosphor/insulator interfaces. PDP aging experiments show that the ALE (Cl) phosphor degrades much faster and more dramatically than the ALE (DEZ) film. Vlasenko and co-workers find evidence from PDP experiments that Cl_s^+ in ALE (Cl) ZnS:Mn ACTFEL devices exists at an energy depth of ~ 0.3 eV. They also find evidence for a trap in ALE (DEZ) ZnS:Mn ACTFEL devices at an energy depth of $\sim 0.9-1.2$ eV that they attribute to oxygen.

Additionally, Vlasenko and co-workers have employed PDP to assess ALE SrS:Ce ACTFEL

devices. [62] At least four PDP bands are evident in the energy range of ~ 1.5 - 2.4 eV in addition to a Ce-related band at ~ 2.8 eV. Evidence for the formation of a negative space charge region in the bulk of the SrS phosphor for applied voltages below threshold is presented and is attributed to the capture of electrons at traps ~ 1.2 - 1.8 eV below the conduction band minimum. However, for applied voltages above threshold, positive space charge in the phosphor dominates and is attributed to the high-field ionization of even deeper traps. PDP spectra of SrS:Ce ACTFEL devices are found to change as the devices are aged; these changes are interpreted as indicating that the conductance of the SrS:Ce film increases during aging.

3 STANDARD ELECTRO-OPTIC CHARACTERIZATION

From a display application point-of-view, the primary properties of importance of an ACTFEL device are the light output, the power required to generate that light, and the color of the light. Hence, the most commonly used techniques to compare and contrast ACTFEL devices worldwide are measurements that explore the luminance (or brightness), the efficiency, and the color spectrum of an ACTFEL device. These three measurements are examined in closer detail in the remainder of this section.

3.1 Luminance-Voltage Characterization

The universal measurement performed on ACTFEL devices in ACTFEL characterization laboratories worldwide is the luminance-voltage (L-V) measurement (sometimes referred to as a brightness-voltage, or B-V, measurement). The basic idea of the L-V measurement is to apply waveforms of steadily increasing amplitude to an ACTFEL device and measure the luminance at each successive amplitude. The L-V measurement proceeds by first applying a voltage waveform with amplitude below the threshold voltage of the device and allowing the device to reach steady-state (usually the

time required to apply several hundred pulses). Then, after the device has reached steady-state, the luminance is measured with a photometer, photomultiplier tube, or photodiode. This luminance measurement reports the luminous intensity output in a direction normal to the emitting surface, and is generally reported in either foot-Lamberts or candelas per square meter. This process is then repeated at successively higher voltage amplitudes until a predetermined stopping voltage. Once the data is collected, the L-V curve is obtained by plotting the voltages on the x-axis and the corresponding luminances on the y-axis, as shown in Fig. 2.

The L-V measurement is very sensitive to the driving waveform, so additional information about the parameters describing the driving waveform should be included. First, the measured luminance depends on the type of waveform used to drive the ACTFEL device. The various laboratories that test ACTFEL devices worldwide often use different types of driving waveforms. The most popular waveforms for performing L-V measurements are sine waves and bipolar trapezoidal waveforms, although some researchers prefer triangle waves. Next, the measured luminance depends to some degree on the rise time, fall time, and pulse width when bipolar trapezoidal waveforms are used to generate L-V data. Finally, the most important driving waveform parameter in terms of the output luminance is the frequency of the driving waveform. The measured luminance at a fixed voltage increases quite noticeably with increasing frequency. This increase is easily reconciled by the fact that at higher frequencies, more pulses are applied to the ACTFEL device per unit time, hence, the luminescent impurities are excited more often. Unfortunately, there is a point of diminishing return with increasing frequency where the luminance either saturates or decreases at a certain frequency. This effect has to do with both device heating and the de-excitation time of the luminescent impurities. When the device heats up, the probability of de-excitation via non-radiative recombination (phonons) is significantly increased, leading to reduced light output. Additionally, luminescent impurities do not decay instantaneously from their excited state to their

ground state; they have some characteristic time associated with this process. When the period of the driving waveform is of the same order as the characteristic decay time of the luminescent impurity, there may be little or no increase in luminance with increasing frequency because many luminescent impurities may already be excited when the following pulse arrives. Essentially, the fraction of time per second that the driving waveform spends above the turn-on voltage determines the relative luminance of the device.

Many materials parameters other than the chemical composition of the phosphor layer contribute to the L-V characteristics of an ACTFEL device. The thickness of the phosphor layer is one parameter that affects the observed luminance of the ACTFEL device. As the phosphor layer of an ACTFEL device becomes thicker (given a fixed doping concentration), a greater number of luminescent impurities are incorporated into the phosphor layer, and a transiting electron has a greater probability of impact excitation. Therefore, with all else being equal, ACTFEL devices with thicker phosphor layers will exhibit greater luminance than thinner devices. Additionally, a greater phosphor thickness leads to a smaller phosphor capacitance, resulting in a greater percentage of the applied voltage being dropped across the phosphor layer. The main drawback to increased phosphor thickness is that a greater applied voltage is required to achieve the threshold electric field in the phosphor. In fact, extremely thick devices may have threshold voltages too large to be turned on with conventional measurement setups. This in turn affects device reliability, because there is a much greater chance of arcing and device burnout when driven at very high voltages. The insulators affect the luminance characteristics of an ACTFEL device mainly through their effect on the voltage distribution through the device. An increase of the insulator capacitance with respect to a fixed phosphor capacitance results in a greater percentage of the applied voltage being dropped across the phosphor layer, which leads to a lower threshold voltage. The two methods of increasing the insulator capacitance are to either decrease the thickness of the insulator layers or

use an insulating material with larger dielectric constant. This is sometimes practical, but the limitation is that essentially all of the applied voltage above the turn-on voltage of an ACTFEL device is dropped across the insulators, requiring high dielectric strength insulators. This is complicated by the fact that high dielectric constant insulating materials tend to have relatively low dielectric strength.

Another materials parameter that is critical in determining the L-V characteristics of an ACTFEL device is the doping level of the luminescent impurity into the phosphor layer. At low dopant concentrations ($\leq 1\%$ for most phosphor materials), the observed luminance increases monotonically with increasing luminescent impurity concentration. Then, an optimum luminance is achieved, and the luminance declines with increasing luminescent impurity concentration above this doping level. This decline is due to the disruption of phosphor crystallinity and the increased number of non-radiative transition paths that result from high luminescent impurity doping levels. [1] Furthermore, at higher luminescent impurity doping levels, hysteresis in the L-V characteristics is sometimes observed. Generally, this hysteresis is such that the light emission from the ACTFEL device is extinguished at a much lower voltage than the threshold voltage. Throughout the literature, this effect has been linked to the phenomenon of positive space charge build-up in the phosphor bulk. [38] This effect presents practical problems in terms of product operation because of contrast reduction when there is difficulty turning display pixels off. However, it has been postulated in the literature that this effect could be useful for some sort of dynamic memory function. [63]

3.2 Efficiency-Voltage Characterization

Another important ACTFEL characterization measurement from an industrial point-of-view is the efficiency-voltage (η -V) measurement. When considering an ACTFEL process for production, an important consideration is power consumption because flat-panel displays are often intended to

run from batteries. Therefore, product engineers are interested in the amount of light that can be produced per unit of power input, or luminous efficiency, η . The luminous efficiency of an ACTFEL device is usually reported in lumens per watt, and is computed from

$$\eta = \pi \frac{L}{P}, \quad (1)$$

where L is the measured luminance in cd/m^2 and P is the applied power density in W/m^2 [1]. The factor of π in Eq. 1 accounts for the assumption of a perfectly diffuse emission surface of the ACTFEL device under test. This assumption is necessary because the luminance measured from a L-V measurement represents only the light emitted normal to the surface of the ACTFEL device, whereas the desired quantity is the luminous intensity integrated over all viewable angles. The η -V measurement is usually performed concomitant with the L-V measurement because the only additional variable that must be measured is the input power density which is computed from

$$P = \frac{1}{A\tau} \int_t^{t+\tau} v(t')i(t')dt', \quad (2)$$

where A is the device area, τ is the period of the driving waveform, and $v(t)$ and $i(t)$ are the applied voltage and current waveforms, respectively. An η -V curve for an evaporated ZnS:Mn device is shown in Fig. 3. The shape of the curve shown in Fig. 3 is typical of most ACTFEL devices.

The η -V measurement depends on many of the same factors as the L-V measurement because η is computed using the luminance data from the L-V curve as one of the input variables. However, because the power requirements for different driving waveforms may change in a different manner than the luminance, η -V curves show some very different trends than L-V curves. One of these different trends is that the η -V curve generally drops with increasing frequency, even for quite moderate frequencies because power density requirements increase more rapidly than the luminance output. The efficiency of an ACTFEL device also depends on the nature of the driving waveform.

An ACTFEL device is most efficient during the rising edge portion of the applied waveform, and least efficient when the voltage is held constant above the threshold voltage. This leads to the conclusion that a triangle wave is the most efficient waveform, whereas a square wave is the least efficient. Another factor that affects ACTFEL device efficiency is space charge. The presence of positive space charge leads to regions of the phosphor layer with very high fields, and regions of the phosphor with very low fields. This seems to affect efficiency in an adverse way because only the high-field portion of the phosphor efficiently emits light. [64] Finally, η depends on the phosphor thickness, because both device luminance and power consumption depend to a large degree on the phosphor thickness. Thin phosphor layers consume the least power, but also produce the least luminance, whereas thick phosphors produce the most luminance, but consume large amounts of power. Therefore, there is an optimum phosphor thickness for maximum efficiency that generally lies between 0.5 and 1 μm for most of the common phosphor materials.

3.3 CIE Color Coordinates

In 1931, the Commission Internationale de l'Eclairage established an international standard for quantifying all visible colors, known as CIE color coordinates. The CIE coordinates are obtained by first computing the three CIE tristimulus values, X, Y, and Z, and subsequently computing the CIE coordinates, x and y, from these values. The CIE tristimulus values are obtained by integrating the product of the spectrum of the light source in question, $P(\lambda)$, and CIE color matching functions, $x_\lambda(\lambda)$, $y_\lambda(\lambda)$, and $z_\lambda(\lambda)$, shown in Fig. 4 over the visible range of wavelengths. [65]

However, in practice, spectra are measured as a discrete set of points, so the integrations are

replaced by the sums,

$$X = \Delta\lambda \sum_{\lambda=\lambda_{violet}}^{\lambda_{red}} x_{\lambda}(\lambda)P(\lambda) \quad (3)$$

$$Y = \Delta\lambda \sum_{\lambda=\lambda_{violet}}^{\lambda_{red}} y_{\lambda}(\lambda)P(\lambda) \quad (4)$$

$$Z = \Delta\lambda \sum_{\lambda=\lambda_{violet}}^{\lambda_{red}} z_{\lambda}(\lambda)P(\lambda), \quad (5)$$

where $\Delta\lambda$ is the interval between points. Then, once X, Y, and Z are obtained, the CIE color coordinates, x, y, and z are calculated from

$$x = \frac{X}{X + Y + Z} \quad (6)$$

$$y = \frac{Y}{X + Y + Z} \quad (7)$$

$$z = \frac{Z}{X + Y + Z}. \quad (8)$$

However, because

$$x + y + z = \frac{X + Y + Z}{X + Y + Z} = 1, \quad (9)$$

only two of the three CIE color coordinates are independent. Therefore, the CIE color coordinates are completely specified from knowledge of the x and y values, and hence, only the x and y CIE color coordinates are typically reported.

Plotting of the CIE y color coordinate versus the CIE x color coordinate over the visual range of light leads to a horseshoe shaped diagram known as the CIE chromaticity diagram. A black and white representation of this diagram is shown in Fig. 5.

The large dot in the center of the CIE chromaticity diagram shown in Fig 5 represents white light, and is located at the CIE color coordinate $x = 0.333$, $y = 0.333$. Then, when the CIE coordinates of a color are specified, the dominant wavelength of the color is the intersection of the line connecting these CIE coordinates and those of white light with the upper arc of the diagram.

[66] This process is depicted in Fig. 6 for a hypothetical color, C_1 , with dominant wavelength C_2 .

Also, the color purity of color C_1 is obtained by taking the ratio of the lengths of the line segments $\overline{CC_1}$ and $\overline{CC_2}$. [66] Furthermore, when the light emission from phosphors of two colors are mixed, the range of colors that it is possible to produce by mixing of these two colors is given by the line that ties the CIE coordinates of these two colors together. [66] For example, the range of colors available by mixing phosphors with CIE color coordinates given by C and C_1 in Fig. 6 is given by the line segment $\overline{CC_1}$. This range of colors is referred to as the color gamut of C_1 and C_2 .

The CIE color coordinates are most useful for the optical characterization of ACTFEL devices as guidelines to gauge the quality of the chromaticity available from a full-color display utilizing the ACTFEL device in question. The color gamut spanned by phosphors of three different colors is obtained by plotting the CIE coordinates of these three colors, and the colors falling within the area of this triangle are included in the color gamut. [67] This is illustrated in Fig. 7 for three hypothetical phosphors of colors C_1 , C_2 , and C_3 .

CIE coordinates are an extremely powerful concept because they facilitate representing an entire luminescent spectrum by two numbers. Furthermore, the simplicity of the visual method for obtaining the color gamut of a set of phosphors is quite attractive. The main drawback to the CIE coordinate system is the complexity involved in their calculation. Fortunately, CIE coordinates are automatically calculated by most modern spectrophotometers, and in the worst case can be calculated by a computer program.

4 NON-STANDARD ELECTRO-OPTIC CHARACTERIZATION

4.1 Photo-Induced Charge and Luminescence Measurements

Photo-induced transferred charge (PIQ) and photo-induced luminescence (PIL) measurements have been employed by several groups for the characterization of ACTFEL devices. [50, 64, 68, 69, 70,

71, 72, 73, 74, 75] PIQ and PIL experiments involve the creation of electron-hole pairs (generated by a short ultraviolet laser pulse) in the phosphor near one of the phosphor/insulator interfaces, transport of this photo-induced charge across the phosphor (aided by the application of a DC voltage across the ACTFEL stack), and measurement of the charge transferred across the phosphor layer or the luminescence emitted from the phosphor layer, respectively, as a function of the magnitude of the applied DC voltage.

PIQ/PIL measurements were originally developed by Corlatan et al. who analyzed evaporated ZnS:Mn ACTFEL devices with probe layers in which only certain regions of the phosphor were Mn-doped. [64, 68] One of the advantages of PIQ/PIL experiments is that electron and hole transport may be studied independently by simply changing the polarity of the DC bias. Corlatan et al. concluded that in ZnS:Mn ACTFEL devices hole transport may give rise to impact excitation-induced electroluminescence, holes are approximately half as efficient as electrons in contributing to the transferred charge, and that the efficiency of transport (where efficiency is defined as PIL divided by PIQ) is significantly greater for holes than electrons. Their conclusion that the photo-induced hole efficiency is greater than the photo-induced electron efficiency was very surprising to them; they interpreted this result as arising from differences in the electric field profile in the phosphor for the cases of hole and electron transport. As discussed in the following, further studies suggest that hole transport is not effective in ZnS, and that what appears to be hole-induced effects are actually due to hole trapping-induced back injection of electrons. [73, 75]

The Heinrich-Hertz Institute (HHI) group has employed PIQ/PIL measurements for the characterization of transport in multi-source deposited SrS:Ce ACTFEL devices. [50, 69, 70, 71, 72] They find no evidence for hole transport in their devices. Thus, carrier transport in SrS:Ce ACTFEL devices is dominated by electrons. PIQ/PIL trends point to the important role of dynamic space charge in determining the behavior of SrS:Ce devices. Furthermore, PIQ/PIL measurements

provide evidence for electron multiplication in SrS at fields significantly below that of the normal ACTFEL threshold. This electron multiplication is attributed to defect ionization.

The basic idea underlying a PIQ/PIL measurement is illustrated in Fig. 8. First, an applied DC voltage pulse is applied to the ACTFEL device to establish the band-bending shown. Next, electron-hole pairs are generated within $\sim 40\text{-}60$ nm [68] of the incident phosphor surface by an ultraviolet laser pulse. The polarity of the applied voltage pulse determines whether electron or hole transport is expected to dominate. The PIQ signal is determined as the transferred charge across a sense capacitor connected in series with the ACTFEL device. The magnitude of the PIQ signal is established by the number of photo-generated carriers and the distance that each carrier travels. The PIL signal is the measured luminescence due to the photo-induced carriers transiting the phosphor. Details of the PIQ/PIL experimental set up and procedure may be found in references [73, 74, 75].

4.1.1 Evaporated ZnS:Mn ACTFEL Device PIQ/PIL Results

All of the data presented in this section is for evaporated ZnS:Mn ACTFEL devices. [73, 75]

Figure 9 is a PIL curve for an ACTFEL device with a phosphor thickness of 950 nm. A distinct PIL threshold is evident at a phosphor field of approximately 1 MV/cm. This threshold corresponds to the average phosphor field at the onset of either: (i) band-to-band impact ionization or (ii) Mn impact excitation. We prefer to attribute the measured PIL threshold to (i) since there is no PIQ or PIL evidence for a second threshold corresponding to the onset of band-to-band impact ionization and we believe that an important condition for efficient ACTFEL operation is that the threshold field for band-to-band impact ionization be less than or equal to the threshold for impact excitation, thus leading to electron multiplication of electrons sourced from interface states. Additionally, the PIL curve shown in Fig. 9 has a base line offset which is due to the photo-luminescence (PL)

response of the device. The PL response is the light produced by the laser exciting the phosphor in the absence of an electric field-induced response. Also note in Fig. 9 that a PIL threshold is observed for holes as well as electrons. This threshold is attributed to a hole trapping-induced back-injection of electrons from the opposite interface, as sketched in Fig. 10. [73, 75] Thus, the hole PIL signal shown in Fig 9 is an artifact which does not actually arise from hole transport. Finally, observe that the PIL signal peaks and then decreases at increasing voltages. This is also believed to be an artifact arising from the difference curve analysis used to estimate PIL. Therefore, the data points for voltages greater than that of the peak voltage are not meaningful and the PIL peak is not significant.

The PIQ curves shown in Fig. 11 for the ACTFEL device with a phosphor thickness of 950 nm are interesting in several respects, as discussed in the following paragraphs.

First, it is puzzling why the electron PIQ signal increases monotonically over the entire range of the maximum applied voltage. Since the PIQ signal magnitude is determined by the number of carriers transported times the distance that they travel before being trapped, one would expect the PIQ signal to saturate at small applied voltages below threshold, once a sufficiently large drift field is established to move the photo-induced carriers across the phosphor layer. Indeed, this type of low-voltage saturation is observed in most of the SrS ACTFEL devices discussed in Section 4.1.2. The monotonically increasing nature of the electron PIQ signal is attributed to a voltage-dependence of carrier extraction from the photo-induced electron-hole plasma. [73, 75] In other words, when a larger voltage is applied, more carriers are extracted from the electron-hole plasma recombination region before they have a chance to recombine, leading to the lack of saturation of the PIQ curves.

The second interesting feature of the PIQ curve shown in Fig. 11 is that the slope of the hole PIQ curve is smaller than the slope of the electron PIQ curve below ~ 125 V (~ 0.8 MV/cm). This

suggests that holes are not as efficient as electrons at traversing the phosphor for fields below ~ 0.8 MV/cm. In contrast, above ~ 125 V the electron and hole PIQ curve slopes are identical. The identical PIQ slopes above ~ 125 V is attributed to hole trapping and back-injection of electrons, as discussed in the previous paragraph. Moreover, if hole trapping is postulated to account for differences in the PIQ electron and hole PIQ slopes for fields below ~ 0.8 MV/cm, it is possible to estimate the following quantities: [73, 75] a trapped hole concentration of $\sim 1-5 \times 10^{17} \text{ cm}^{-3}$, a hole drift length of $\sim 180 \pm 70$ nm, a hole lifetime of ~ 2 ps, and a hole trap capture cross-section of $\sim 7 \times 10^{-13} \text{ cm}^2$. The extremely large magnitude of this hole capture cross section is particularly revealing since it corresponds to a negatively charged deep level trap whose charge state leads to very efficient hole capture because of the coulombically attractive interaction between the trap and the hole. It is likely that this hole trap is a defect complex involving a zinc vacancy.

4.1.2 SrS ACTFEL Device PIQ/PIL Results

Three types of SrS ACTFEL devices are discussed in this section: ALE-deposited SrS:Ce, sputtered SrS:Cu, and undoped metal-organic chemical vapor (MOCVD) deposited SrS ACTFEL devices. [74]

One comment regarding the experimental procedure used for assessing SrS ACTFEL devices is warranted. An important requirement for obtaining reliable PIQ/PIL data is to ensure that the ACTFEL device is 'reset' before each PIQ/PIL measurement pulse to a flat-band state. This requires that all of the residual bulk space and polarization charge generated during the preceding pulse must be annihilated. For ZnS:Mn ACTFEL devices, this is readily accomplished using an 'optical reset' which is a broad-band UV light pulse incident through the ITO interface [68, 73, 75]. The UV light creates electron-hole pairs within the phosphor that are free to drift throughout the phosphor and recombine with residual charge, thus achieving energy bands close to flat-band, or

at least achieving a reproducible state. However, we have found this 'optical reset' procedure to be inadequate for properly resetting most SrS ACTFEL devices, presumably because they typically possess much more space charge than ZnS:Mn ACTFEL devices. Thus, a more complex 'electro-optic reset' procedure is employed for the SrS results presented in this section. [74] Briefly, this 'electro-optic reset' procedure consists of applying an amplitude-ramped 1 kHz sinusoidal voltage waveform to the ACTFEL device during the optical reset pulse.

PIQ curves for a 1100 nm thick SrS:Ce ACTFEL device are shown in Fig. 12. For the electron PIQ curve, the PIQ signal increases and exhibits low-field saturation at ~ 0.3 MV/cm, begins gradually rising at ~ 0.8 MV/cm (denoted Threshold 1), and then dramatically rises at ~ 1.1 MV/cm (denoted Threshold 2). No true hole PIQ signal is observed in Fig. 12 or in any of the SrS:Ce ACTFEL devices tested; the small hole PIQ signal displayed is actually an artifact of the difference curve analysis used. [74]

PIL curves for a 1100 nm thick SrS:Ce ACTFEL device are shown in Fig. 13. First, up to ~ 90 V (~ 0.5 MV/cm), the electron PIL intensity decreases (such a decrease is not seen in ZnS:Mn PIL curves). This decrease is explained as follows. Hole trapping is extraordinarily effective in SrS:Ce such that photo-induced holes are immediately trapped. For small applied voltages, the phosphor field is too small to separate electrons from trapped holes so that photo-induced electrons radiatively recombine, leading to a strong PL signal. Larger applied voltages result in more separation of electron-hole pairs, reducing the PL intensity. Next, the electron PIL curve begins gradually rising at ~ 0.8 MV/cm (denoted Threshold 1) and then dramatically increases at ~ 1.1 MV/cm (denoted Threshold 2), in a similar fashion as that shown in the PIQ curve of Fig. 12. Finally, there is no discernible PIL threshold for holes in any SrS:Ce sample tested.

PIQ curves for a 1100 nm SrS:Cu ACTFEL device are shown in Fig. 14. These PIQ curves are similar to those shown in Fig. 12 for SrS:Ce ACTFEL devices, except that the low-field saturation

is not distinct for the SrS:Cu device. Note that SrS:Cu samples exhibit a weak threshold (Threshold 1) at ~ 0.8 MV/cm, which rises to a significantly stronger main threshold (Threshold 2) at ~ 1.1 MV/cm. There is no discernible hole PIQ signal for this or any of the other SrS:Cu ACTFEL devices studied.

PIL curves for a 1100 nm thick SrS:Cu ACTFEL device are presented in Fig. 15. PIL trends are similar to those observed for SrS:Ce ACTFEL devices (i.e. decreasing PL signal with increasing voltage, strong threshold at ~ 1.2 MV/cm (Threshold 2)) except that there is no evidence of a weak threshold (i.e. Threshold 1) for either of the two SrS:Cu ACTFEL devices assessed in this study.

PIQ curves for a 400 nm thick undoped SrS ACTFEL device are presented in Figure 16. There are two major differences between the doped and the undoped PIQ results. First, and most surprising, is evidence of hole transport. This suggests that luminescent impurity doping of the SrS phosphor creates traps that prevent holes from efficiently being transported across the phosphor layer. The second major difference between PIQ results of doped and undoped samples is the lack of saturation of the electron PIQ signal for the undoped SrS ACTFEL device. This is similar to what is seen for ZnS:Mn ACTFEL devices (see Fig. 11) and, thus, is rationalized in the same manner (i.e. the lack of PIQ low-field saturation is ascribed to a voltage-dependence of carrier extraction from the photo-induced electron-hole plasma). Note that this explanation implies that PIQ low-field saturation only occurs for intense hole trapping.

In summary, the PIQ/PIL results presented in this section provide evidence for a weak threshold at ~ 0.8 MV/cm (Threshold 1) and a strong threshold at ~ 1.1 MV/cm (Threshold 2) for SrS:Ce and SrS:Cu ACTFEL devices, which are prepared using different phosphor deposition methods (ALE and sputtering, respectively). Threshold 2 is evident in both PIQ and PIL curves for both types of ACTFEL devices, whereas Threshold 1 is not observed in PIL curves for SrS:Cu ACTFEL devices. Assuming tunnel injection from a trap, a ~ 0.8 MV/cm (~ 1.1 MV/cm) field corresponds to a trap

depth of ~ 0.6 eV (~ 0.9 eV). Threshold 1 is most likely associated with the ionization of traps in the phosphor layer. [50] Since Threshold 1 is found in two different types of ACTFEL devices, it is likely that the trap associated with Threshold 1 arises from an intrinsic defect or from an omnipresent impurity; likely candidates are a sulfur vacancy (a double donor) or an oxygen sitting on a sulfur site (an isoelectronic, acceptor-like trap). Strong Threshold 2 probably corresponds to the onset of impact ionization. Finally, the absence of PIQ saturation and the existence of hole transport in undoped SrS ACTFEL devices are strong evidence that the dominant hole traps in doped SrS ACTFEL devices are luminescent impurity-induced; likely candidate luminescent impurity-induced trap states are a strontium vacancy-Ce_{Sr} defect complex (a double donor-single acceptor complex) and Cu_{Sr} (an acceptor).

4.2 Subthreshold Voltage-Induced Transferred Charge Analysis

Subthreshold voltage-induced transferred charge (VIQ) is a useful technique for investigating subtle device physics electrical operation and the aging behavior of ACTFEL devices. [73, 74, 76] The VIQ set-up is shown in Fig. 17. The VIQ experiment consists of applying a large number (typically 20,000) of bipolar trapezoidal voltage pulses of a variable subthreshold voltage amplitude and monitoring the polarity and magnitude of the voltage induced across a sense capacitor during illumination of the ACTFEL device with a xenon lamp to optically reset the voltage-induced space charge within the ACTFEL device; this induced voltage across the sense capacitor during the optical reset is the VIQ signal.

A VIQ timing diagram is shown in Fig 18 and illustrates the origin of the VIQ signal. A VIQ curve is obtained by plotting the VIQ signal versus the applied voltage amplitude from 0 V up to threshold. Such VIQ plots typically consist of one or more gaussian-shaped peaks. The voltage location, height, polarity, and temperature dependence of a VIQ peak provides information about

the physical location, energy depth, capture cross-section, and density of phosphor traps giving rise to the VIQ signal. Moreover, changes in the VIQ signal as a function of aging time provide information related to the physical nature of ACTFEL aging.

The essence of VIQ may be discerned with the aid of Figs. 19 and 20, which show two possible VIQ energy band diagrams during the optical reset portion of the experimental sequence when the VIQ signal is monitored as the maximum transient voltage developed across the sense capacitor. The VIQ space charge distribution in Fig. 19 [Fig. 20] shows negative charge near the bottom (ITO) [top (Al)] interface and positive [negative] charge near the top (Al)[bottom (ITO)] interface. When the device is flooded with above-bandgap photons following application of the bipolar voltage pulse sequence, the photo-injected electron-hole pairs generated in the phosphor are transported subject to the internal phosphor field established by space charge within the ACTFEL device. The VIQ polarity is established by the direction of flow of the photo-generated carriers, as illustrated in Figs. 19 and 20. Note that the existence of a non-zero VIQ signal is evidence for space charge asymmetry within the phosphor due to the applied subthreshold voltage.

4.2.1 ZnS:Mn ACTFEL Device VIQ Results

ZnS:Mn VIQ aging experiments are performed using samples with phosphors deposited by three different methods: thermal evaporation, ALE (Cl), and ALE (DEZ). [73, 76] The method of deposition has a strong effect on the aging characteristics of the ACTFEL device.

VIQ aging curves for a thermally evaporated ZnS:Mn ACTFEL device are shown in Fig. 21. A negative polarity VIQ peak occurs for the first few hours of operation; this corresponds to a situation in which the most shallow VIQ traps are located near the bottom (ITO) interface; this gives rise to positive charge near the bottom interface, as shown in Fig. 20. The negative VIQ peak initially increases in magnitude and then decreases in magnitude as a function of aging, with

the location of the voltage peak increasing slightly. After ~ 40 hours of aging at 1 kHz, the VIQ polarity switches from negative to positive. A positive VIQ peak is attributed to localization of the most shallow VIQ traps near the top (Al) interface, giving rise to positive charge near the top (Al) interface, as shown in Fig. 19. The voltage at which the VIQ peaks gradually decreases for aging periods longer than 40 hours. The VIQ response exhibits a VIQ threshold voltage of ~ 90 V, corresponding to a VIQ threshold field of ~ 0.7 MV/cm, which remains constant with aging. The fact that the VIQ threshold field does not change with aging suggests that the VIQ traps at the top and bottom interface arise from the same type of trap. The decrease and subsequent switch of polarity with aging is attributed to changes in the trap density at or near the interfaces. The increase in the VIQ peak magnitude for initial aging is attributed to generation of more traps near the bottom (ITO) interface. Later aging causes generation of traps near the top (Al) interface, resulting in a reduction of the VIQ maximum, and finally leading to a switch in the VIQ polarity.

L-V and capacitance-voltage (C-V) measurements of evaporated ZnS:Mn ACTFEL devices exhibit p-shift followed by n-shift aging characteristics. [73, 77] These L-V and C-V p-shift to n-shift aging trends correlate well with VIQ measurements in which the negative polarity VIQ signal switches to a positive polarity VIQ signal for longer aging periods. Thus, these L-V, C-V, and VIQ aging trends arise from a common source.

VIQ aging curves for an ALE (Cl) ZnS:Mn ACTFEL device are shown in Fig. 22. The unaged ALE (Cl) samples have a single small negative VIQ peak and develop two large negative peaks with aging. A negative polarity VIQ signal is consistent with the energy band diagram shown in Fig. 20, in which the most shallow VIQ trap states are present near the bottom (ITO) interface. The lower voltage peak, Peak 1, grows with aging and remains at the same voltage. The trap responsible for Peak 1 must be very shallow since the VIQ threshold voltage occurs at approximately 0 V. The higher voltage peak, Peak 2, grows and shifts to a lower voltage with aging. Peak 2 is attributed

to a deeper trap. VIQ aging does not appear to stabilize, although the rate of growth of both VIQ peaks slows down after the ACTFEL device has been aged for a long time.

VIQ aging curves for an ALE (DEZ) ZnS:Mn ACTFEL device are shown in Fig. 23. A single VIQ peak is observed which initially increases and then decreases in magnitude. The VIQ peak voltage decreases with aging. A positive polarity VIQ curve is consistent with the energy band diagram shown in Fig. 19 in which the most shallow VIQ traps are present at or near the top (Al) interface. The initial increase in the VIQ magnitude is likely due to an increase in the number of traps responsible for VIQ near the top (Al) interface. The subsequent decrease in VIQ magnitude and concomitant shift in the peak to a lower voltage after 4 hours of aging is possibly due to generation of traps at the bottom (ITO) interface. Further evidence for the presence of a VIQ trap at the bottom (ITO) interface is presented below.

The trap depth and capture cross-section of a VIQ trap may be estimated from temperature-dependent VIQ analysis, [73, 76] as summarized in Table 1, and may also provide clues regarding the atomic identification of VIQ traps. Traps with a capture cross-section greater than $\sim 10^{-14} \text{cm}^2$ are coulombically attractive, traps with a capture cross-section of $\sim 10^{-14} - 10^{-18} \text{cm}^2$ are neutral, and traps with a capture cross-section less than $\sim 10^{-18} \text{cm}^2$ are coulombically repulsive. [78] Thus, the capture cross-section of the evaporated ZnS:Mn VIQ trap indicates this trap to be attractive or neutral and the ALE (DEZ) VIQ trap to be neutral. A likely candidate for the evaporated ZnS:Mn VIQ trap would be a sulfur vacancy, which is a double donor that would be coulombically attractive to electron capture. Also, the first and second ionization energies of a sulfur vacancy in ZnS have been estimated as ~ 1.2 and ~ 1.4 eV, [79] in reasonable agreement with the VIQ trap energy depth estimate. A possible ALE (DEZ) VIQ trap would be oxygen on a sulfur site, which is an isoelectronic trap, [80] and would hence be neutral for electron capture. Finally, the energy depth of Cl in ZnS is $\sim 0.2 - 0.3$ eV, [81, 82, 83] suggesting that VIQ Peak 1 in the ALE (Cl) ZnS:Mn

ACTFEL device is due to Cl.

4.2.2 SrS: ACTFEL Device VIQ Results

Three types of samples are considered in this section: ALE-deposited SrS:Ce, sputter-deposited SrS:Cu, and MOCVD-deposited undoped SrS ACTFEL devices. [74]

VIQ temperature-dependent curves for a 850 nm thick SrS:Ce ACTFEL device are presented in Fig. 24. The VIQ curves are all of positive polarity, indicating that the most shallow VIQ traps exist near the top (Al contact) insulator/phosphor interface. Also note that the VIQ threshold voltage is very small; thus, this VIQ trap is extremely shallow.

Temperature-dependent VIQ curves for a 1100 nm thick SrS:Cu ACTFEL device are presented in Fig. 25. Two important trends are evident. First, all VIQ curves exhibit a negative polarity, implying that the most shallow traps are located near the bottom (ITO) insulator/phosphor interface. Second, the VIQ threshold decreases with increasing temperature, which allows the VIQ trap depth and capture cross-section to be estimated.

Temperature-dependent VIQ measurements for a 400 nm undoped SrS ACTFEL device are shown in Fig. 26. The unique feature of these curves is the existence of a temperature-dependent VIQ voltage bipolarity near the VIQ threshold. Since all of the VIQ curves are primarily positive in polarity, a larger density of VIQ traps is present near the top (Al contact) insulator/phosphor interface. For the 30 and 150 K curves, however, there is a slight negative polarity portion of the VIQ curve, suggesting that shallower traps located near the bottom (ITO contact) insulator/phosphor interface are dominant. Note that the VIQ threshold voltage is identical for both the positive and the negative polarity curves shown in Fig. 26; this suggests that the same kind of trap is responsible for both the positive and the negative polarity VIQ thresholds, but that these traps are located at opposite interfaces.

Trap depths and capture cross-sections estimated from temperature-dependent VIQ analysis, as well as possible VIQ trap atomic identifications, are summarized in Table 2. The donor ionization level of the Ce_{Sr} luminescent impurity is considered to be a likely candidate for the very shallow SrS:Ce VIQ trap. The coulombically attractive nature and trap depth energy of 0.9 eV suggests the second ionization state of a sulfur vacancy (a double donor) as a possible VIQ trap identification for the SrS:Cu phosphor. The first ionization state of a sulfur vacancy or an O_S isoelectronic trap are suggested as possibilities for the undoped SrS phosphor.

4.2.3 Lanthanide Doping Studies

Lanthanide doping studies provide a simple means for assessing the relative high field transport efficiency and short wavelength EL potential of an ACTFEL phosphor. [9, 84, 85] The idea underlying these studies is very simple: intentionally dope the phosphor of interest with appropriate lanthanide luminescent impurities, monitor EL from ACTFEL devices fabricated using these lanthanide-doped phosphors, and evaluate the high field transport efficiency and short wavelength EL potential of the phosphor based on the relative intensity of the high energy EL peaks.

In the original lanthanide doping study, the EL spectra of ZnS and SrS ACTFEL devices prepared in a very similar manner and doped with Dy, Er, Ho, Tb, and Tm were compared. This direct comparison provides evidence that the electron distribution is significantly hotter in SrS than in ZnS, even though the average phosphor field is smaller in SrS. Moreover, the hot electron distribution in ZnS does not appear to be sufficiently energetic to efficiently excite luminescent impurities appropriate for the short wavelength portion of the visible spectrum, as witnessed by the fact that the ZnS EL spectra invariably cuts off at about 480 nm, independent of the luminescent impurity employed. A few selected spectra from this study are shown in Figs. 27-28 and the results of this study are summarized in Table 3.

Figure 27 shows a comparison of the normalized EL spectra of ZnS:Tb and SrS:Tb ACTFEL devices. The most important aspect of Fig. 27 is that the ZnS:Tb EL spectrum shows an abrupt cut off at ~ 470 nm whereas three higher energy transitions are clearly evident in the SrS:Tb spectrum. This is evidence that the hot electron distribution is much more heated above ~ 470 nm (i.e. ~ 2.64 eV) in SrS compared to ZnS.

Figure 28 shows a comparison of the normalized EL spectra of ZnS:Er and SrS:Er ACTFEL devices. The most significant aspect of Fig. 28 is the new EL peaks present in SrS that are not present in ZnS. Of particular consequence is the fact that for SrS the most intense peak is the $^4G_{11/2}$ - $^4I_{15/2}$ UV peak located at about 385 nm (i.e. ~ 3.22 eV); the intensity of this peak suggests that the SrS electron distribution may actually peak at energies corresponding to the UV portion of the electromagnetic spectrum; if true, it is conceivable that the SrS electron distribution is too energetic for optimal ACTFEL performance.

A summary of selected properties of these devices is given in Table 3. The first three columns represent, respectively, an assessment of the relative amount of capacitance-voltage (C-V) overshoot, transferred charge capacitance (dQ_{max}/dV_{max}) overshoot, and trailing edge (TE) luminescence found in each device. These three measurements are useful for estimating the relative amount of positive space charge present in these devices. [84] The fourth column of Table 1 shows the steady-state phosphor field (F_{ss}) as estimated via Q- F_p analysis for an applied voltage of 40 V above threshold. Finally, the last three columns of Table 1 include the luminance (L) at 40 V above threshold and 1000 Hz (except for ZnS:Tm which is so dim that a frequency of 5000 Hz is used), and the color coordinates (CIE $_x$, CIE $_y$) for ZnS and SrS ACTFEL devices doped with various lanthanide luminescent impurities.

Analysis of Table 3 allows one to observe some interesting trends. First, note that differences in the CIE coordinates of the SrS and ZnS are all consistent with SrS ACTFEL devices having a

'blue shift' in which the spectra are shifted to higher energies; this is consistent with SrS having a hotter electron distribution. Second, all of the ZnS devices have a significantly larger average phosphor field of 1.8-2.1 MV/cm compared to the 1.2-1.45 MV/cm average phosphor field found for SrS ACTFEL devices. Third, the C-V and the $dQ_{max}/dV_{max}-V_{max}$ overshoot trends and the TE luminescence trends are consistent with ZnS ACTFEL devices having very little, if any, positive space charge, whereas all of the SrS ACTFEL devices tested appear to possess some positive space charge. Thus, these results suggest that the electric field is more uniform in ZnS phosphors than in SrS phosphors, since positive space charge seems to always be present in SrS phosphors. Fourth, note that very little, if any, TE luminescence is detected in the ACTFEL devices tested. This implies that the luminescent impurity excitation mechanism for these devices is primarily impact excitation, not impact ionization and that differences in the high energy performance of SrS and ZnS ACTFEL devices cannot be attributed to differences in the luminescent impurity excitation mechanism. Thus, it is concluded that the superior high energy performance of SrS compared to ZnS is due to a more energetic hot electron distribution in SrS compared to ZnS. Moreover, it is likely that at least a portion of this superior high energy performance of SrS arises from its tendency to more readily form positive space charge than ZnS.

In the original lanthanide doping study, a variety of lanthanide luminescent impurities were employed in order to establish the viability of the method. [9, 84] In subsequent studies, only one lanthanide dopant, Ho, is used based on its abundance of high energy EL emission peaks. [85] Figure 29 shows a comparison of the normalized EL spectra of ZnS:Ho, SrS:Ho, BaS:Ho, CaS:Ho, and CaSe:Ho ACTFEL devices. Note that the Ho high energy EL emission peaks are suppressed for the case of ZnS:Ho and CaSe:Ho, but that the spectra for SrS:Ho, BaS:Ho, CaS:Ho are very similar. Thus, the electrons in ZnS and CaSe are not energetic enough to excite the higher energy 5F_1 , 5G_5 , and 5G_4 excited states. It is concluded that ZnS and CaSe are not appropriate phosphors for

blue ACTFEL applications, based on the fact that their hot electron distributions are inadequately heated.

ACKNOWLEDGEMENTS

This work was supported by DARPA under the Phosphor Technology Center of Excellence, Grant No. MDA 972-93-1-0030 and NSF under DMR 0071899.

References

- [1] Y. A. Ono, *Electroluminescent Displays*, World Scientific, Singapore (1995).
- [2] J. F. Wager and P. D. Keir, *Ann. Rev. Mater. Sci.* **27**, 223 (1997).
- [3] J. C. Hitt, J. P. Bender, and J. F. Wager, *CRC Crit. Rev. Solid State Mater. Sci.* **275**, 29 (2000).
- [4] A. H. Kitai, (Ed.), *Solid State Luminescence : Theory, Materials, and Devices*, Chapman and Hall, London (1993).
- [5] E. Bringuier, *J. Appl. Phys. Lett.* **75**, 4291 (1994).
- [6] G. Blasse and B. C. Grabmaier, *Luminescent Materials*, Springer-Verlag, Berlin (1994).
- [7] P.D. Rack and P.H. Holloway, *Mater. Sci. Engr. Reports*, **R21** 171 (1998).
- [8] S. Shionoya and W. M. Yen, (Eds.), *Phosphor Handbook*, CRC Press, Boca Raton, (1999).
- [9] P. D. Keir, Ph. D. Thesis, Oregon State University (1999).
- [10] G. Mueller, (Ed.), *Electroluminescence I (Semiconductors and Semimetals, Vol 64)*, Academic, New York (1999).
- [11] G. Mueller, (Ed.), *Electroluminescence II (Semiconductors and Semimetals, Vol 65)*, Academic, New York (2000).
- [12] D. K. Schroder, *Semiconductor Material and Device Characterization*, 2nd edition, Wiley, New York (1998).
- [13] K-W. C. Yang, Ph. D. Thesis, Oregon State University (1981).
- [14] K-W. C. Yang, *IEEE Trans. Electron Devices* **ED-30**, 452 (1983).
- [15] J. Zheng and J. W. Allen, *Semicond. Sci. Technol.* **9**, 1013 (1990).
- [16] M. Ando and Y. A. Ono, *J. Appl. Phys.* **69**, 7225 (1991).
- [17] P. K. Ghosh and B. Ray, *Prog. Crystal Growth and Charact.* **25**, 1 (1992).
- [18] D. R. Vij, (Ed.), *Thermoluminescent Materials*, PTR Prentice Hall , Englewood Cliffs (1993).
- [19] E. Nakazawa, *Jpn. J. Appl. Phys.* **23**, L755 (1984).
- [20] J. Rennie, E. Nakazawa, and T. Koda, *Jpn. J. Appl. Phys.* **29**, 509 (1990).
- [21] I. F. Chang and P. Y. Yu, *Appl. Phys. Lett.* **32**, 432 (1978).
- [22] V. Marrello, L. Samuelson, A. Onton, and W. Reuter, *J. Appl. Phys.* **52**, 3590 (1981).
- [23] H. Venghaus, *J. Crystal Growth* **59**, 403 (1982).
- [24] H. Kobayashi, S. Tanaka, H. Sasakura, K. Tsujita, and R. Tueta, *Appl. Phys. Lett.* **40**, 1024 (1982).

- [25] R. S. Crandall, Appl. Phys. Lett. **50**, 641 (1987).
- [26] R. S. Crandall, M. Ling, J. Kane, and P. N. Yocom, SID 87 Digest, 245 (1987).
- [27] R. G. Pappalardo and M. Levinson, J. Appl. Phys. **66**, 6189 (1989).
- [28] R. G. Pappalardo, J. Electrochem. Soc. **137**, 3469 (1990).
- [29] M. Ando and Y. A. Ono, J. Appl. Phys. **68**, 3578 (1990).
- [30] M. Ando, Y. Abe, and Y. A. Ono, J. Appl. Phys. **70**, 5018 (1991).
- [31] S. Tanaka, H. Yoshiyama, K. Nakamura, S. Wada, H. Morita, and H. Kobayashi, Jpn. J. Appl. Phys. **30**, L1021 (1991).
- [32] M. Ando and Y. A. Ono, J. Crystal Growth **117**, 969 (1992).
- [33] K. Ohmi, K. Ishitani, S. Tanaka, and H. Kobayashi, J. Appl. Phys. **67**, 944 (1995).
- [34] K. Ohmi, K. Ishitani, Y. Kashio, S. Tanaka, and H. Kobayashi, J. SID **5**, 145 (1997).
- [35] M. Peter, S. Nishimura, M. Murayama, K. Ohmi, S. Tanaka, and H. Kobayashi, J. Appl. Phys. **86**, 7071 (1999).
- [36] S. Tanaka, H. Kobayashi, H. Sasakura, and Y. Hamakawa, J. Appl. Phys. **47**, 5391 (1976).
- [37] D. H. Smith, J. Lumin. **23**, 209 (1981).
- [38] W. E. Howard, O. Sahni, and P. M. Alt, J. Appl. Phys. **53**, 639 (1982).
- [39] P. Thioulouse, J. Crystal Growth **72**, 545 (1985).
- [40] A. A. Douglas, J. F. Wager, D. C. Morton, J. B. Koh, and C. P. Hogh, J. Appl. Phys. **63**, 231 (1993).
- [41] N. E. Rigby and J. W. Allen, J. Phys. C. **21**, 3483 (1988).
- [42] S. Tanaka (Private communication)(1993).
- [43] E. Bringuier and A. Geoffroy, Appl. Phys. Lett. **48**, 1780 (1986).
- [44] S. Tanaka, J. Lumin. **40-41**, 20 (1988).
- [45] S. Tanaka, H. Yoshiyama, Y. Mikami, J. Nishiura, S. Ohshio, and H. Kobayashi, Proc. SID **29**, 77 (1988).
- [46] V. P. Singh and D. C. Morton, IEEE Trans. Electron Devices **ED-36**, 54 (1989).
- [47] V. P. Singh, W. Z. Majid, and D. C. Morton, J. SID **1**, 135 (1993).
- [48] D. C. Morton, J. Koh, C. P. Hogh, and R. Khormaei, Appl. Phys. Lett. **ED-63**, 863 (1993).
- [49] A. A. Douglas, J. F. Wager, D. C. Morton, J. B. Koh, and C. P. Hogh, J. Appl. Phys., **73**, 296 (1993).

- [50] U. Troppenz, B. Huettl, K. O. Velthaus, and R. H. Mauch, *J. Crystal Growth* **138**, 1017 (1994).
- [51] K. Neyts and E. Soininen, *IEEE Trans. Electron Devices* **ED-42**, 51086 (1995).
- [52] P. Bailey, D. Carkner, and X. Wu, *J. Appl. Phys.* **81**, 931 (1997).
- [53] K. W. Yang, S. J. T. Owen, and D. H. Smith, *IEEE Trans. Electron Devices* **ED-28**, 703 (1981).
- [54] M. Ogawa, S. Nakada, M. Sakurai, and T. Yoshioka, *J. Lumin.* **29**, 11 (1984).
- [55] A. Geoffroy and E. Bringuier, *Appl. Phys. Lett.* **67**, 4276 (1990).
- [56] J. Benoit, P. Benalloul, C. Barthou, S. Casette, and J. C. Soret, *Phys. Stat. Sol. (a)* **122**, 427 (1990).
- [57] A. Zeinert, P. Benalloul, J. Benoit, C. Barthou, J. Dreyhsig, and H.-E. Gumlich, *J. Appl. Phys.* **71**, 2855 (1992).
- [58] A. Geoffroy and E. Bringuier, *Appl. Phys. Lett.* **61**, 3172 (1992).
- [59] Y. Kononets, R. Törnqvist, N. Vlasenko, *Inorganic and Organic Electroluminescence*, edited by R. Mauch, H. Gumlich, Wissenschaft an Technik Verlag, Berlin, p. 259 (1996).
- [60] N. Vlasenko, A. Beletskii, Z. Denisova, Y. Kononets, L. Veligura, *Inorganic and Organic Electroluminescence*, edited by R. Mauch, H. Gumlich, Wissenschaft an Technik Verlag, Berlin, p. 267 (1996).
- [61] N.A. Vlasenko, Y. F. Kononets, A. I. Beletskii, Z. L. Denisova, Y. V. Kopytko, E. L. Soininen, R. O. Törnqvist, and K. M. Vasama, *J. SID Suppl.* **1**, 39 (2000).
- [62] N.A. Vlasenko, A. I. Beletskii, Z. L. Denisova, and Y. F. Kononets, *J. SID Suppl.* **1**, 61 (2000).
- [63] W. E. Howard, *J. Lumin.* **23**, 155 (1981).
- [64] D. Corlatan, K. A. Neyts, and P. De Visschere, *J. Appl. Phys.* **78**, 7259 (1995).
- [65] F. W. Billmeyer and M. Saltzman *Principles of Color Technology, 2nd Edition*, Wiley, New York (1981).
- [66] A. C. Hardy, *Handbook of Colorimetry*, The Technology Press, Cambridge, MA (1936).
- [67] R. D. Overheim and D. L. Wagner, *Light and Color*, Wiley, New York (1982).
- [68] D. Corlatan, K. Neyts, P. De Visschere, and J. Van den Bossche, in *Proceedings of 1994 International Workshop on Electroluminescence*, edited by X. Xu, Science Press, Beijing, p. 211 (1994).
- [69] U. Troppenz, B. Huettl, K. O. Velthaus, and R. H. Mauch, in *Proceedings of 1994 International Workshop on Electroluminescence*, edited by X. Xu, Science Press, Beijing, p. 162 (1994).
- [70] B. Huettl, U. Troppenz, K. O. Velthaus, C. R. Rhonda, and R. H. Mauch, *J. Appl. Phys.* **78**, 7282 (1995).

- [71] B. Huettl, P. Kratzert, K. Lite, B. Reinsperger, T. K. Plant, and R. H. Mauch, in *Inorganic and Organic Electroluminescence*, edited by R. H. Mauch and H.-E. Gumlich, Wissenschaft and Technik Verlag, Berlin, p.73 (1996).
- [72] U. Troppenz, T. K. Plant, B. Huettl, K. O. Velthaus, and R. H. Mauch, *J. SID.* **4**, 293 (1996).
- [73] B. A. Cleary, M. S. Thesis, Oregon State University (1998).
- [74] C. A. Nevers, M. S. Thesis, Oregon State University (1999).
- [75] B. A. Cleary, J. C. Hitt, P. D. Keir, T. K. Plant, J. F. Wager, and S. S. Sun, *J. SID Suppl.* **1**, 51 (2000).
- [76] B. A. Cleary, P. D. Keir, J. C. Hitt, T. K. Plant, J. F. Wager, B. Aitchison, R. T. Tuenge, and S. S. Sun, *J. SID* (in press).
- [77] A. Mikami, K. Terada, K. Okibayashi, K. Tanaka, M. Yoshida, S. Nakajima, *J. Appl. Phys.* **72**, 773 (1992).
- [78] B. Ball, G. Barbottin, *Instabilities in Silicon Devices*, edited by G. Barbottin, A. Vappaille, Elsevier, Amsterdam, p. 7 (1989).
- [79] S. Sohn, Y. Hamakawa, *Jpn. J. Appl. Phys.* **31**, 3901 (1992).
- [80] K. Akimoto, H. Okuyama, M. Ikeda, Y. Mori, *Jpn. J. Appl. Phys.* **72**, 773 (1992).
- [81] W. Hoogstraten, *Philips Res. Repts* **13**, 515 (1958).
- [82] C. Kang, P. Phipps, R. Bube, *Phys. Rev.* **156**, 998 (1967).
- [83] H. Arbell, A. Halperin, *Phys. Rev.* **117**, 45 (1960).
- [84] P. D. Keir, C. Maddix, B. A. Baukol, J. F. Wager, B. L. Clark, and D. A. Keszler, *J. Appl. Phys.* **86**, 6810 (1999).
- [85] C. M. Maddix, M. S. Thesis, Oregon State University (2000).

Table 1: VIQ aging summary for ZnS:Mn ACTFEL devices. Possible origin refers to a suggested atomic identification of the VIQ trap of interest, based on its VIQ-assessed trap properties. (From [76], B. A. Cleary et al., J. SID (in press), with permission from the Society for Information Display @ 2001).

Trap Property	Evaporated ZnS:Mn	ALE (Cl) ZnS:Mn	ALE (DEZ) ZnS:Mn
VIQ Polarity	negative (initial aging) positive (later aging)	negative	positive
E_{trap} (eV)	$\sim 1.0-1.2$	~ 0.3 (pk 1) ? (pk 2)	$\sim 0.7-0.9$
σ (cm ²)	$\sim 10^{-13}-10^{-15}$?	$\sim 10^{-14}-10^{-16}$
Coulombic Nature	attractive/neutral	?	neutral
Possible Origin	$V_S^{0/+}$	$Cl_S^{0/+}$ (pk 1)	$O_S^{-/0}$

Table 2: VIQ aging summary for SrS ACTFEL devices. Possible origin refers to a suggested atomic identification of the VIQ trap of interest, based on its VIQ-assessed trap properties. (From Ref. [74], C. A. Nevers, M. S. Thesis, Oregon State University, 1999).

Trap Property	ALE SrS:Ce	Sputtered SrS:Cu	MOCVD SrS (undoped)
VIQ Polarity	positive	negative	bipolar
E_{trap} (eV)	~ 0.1	~ 0.9	~ 0.6
σ (cm ²)	?	$\sim 10^{-13}$?
Coulombic Nature	?	attractive	?
Possible Origin	$\text{Ce}_{\text{Sr}}^{0/+}$	$\text{V}_{\text{S}}^{+/++}$	$\text{V}_{\text{S}}^{0/+}$ or $\text{O}_{\text{S}}^{-/0}$

Table 3: A summary of the amount of capacitance-voltage (C-V) overshoot, transferred charge capacitance (dQ_{max}/dV_{max}) overshoot, and trailing edge (TE) luminescence. The percentages included in the table reflect the peak of the overshoot compared to the insulator capacitance for C-V and dQ_{max}/dV_{max} measurements and the peak intensity of the TE edge luminescence compared to the peak intensity of the leading edge luminescence. Also tabulated is the steady-state phosphor field (F_{ss}), the luminance (L at 40 V above threshold at a frequency of 1000 Hz, except for ZnS:Tm* which is so dim that a frequency of 5000 Hz was used), and the color coordinates (CIE_x, CIE_y) for ZnS and SrS ACTFEL devices doped with various lanthanide luminescent impurities. (From Ref. [84], P. D. Keir et al., J. Appl. Phys. **86**, 6810, 1999, with permission from the American Institute of Physics @ 1999).

Phosphor	C-V Overshoot	dQ_{max}/dV_{max} Overshoot	TE Luminescence	F_{ss} (MV/cm)	L (cd/m ²)	CIE _x	CIE _y
ZnS:Tb	none	none	none	1.9	23.1	0.31	0.59
SrS:Tb	small (10%)	moderate (60%)	yes (10%)	1.45	17.2	0.32	0.55
ZnS:Tm	none	small (10%)	none	2.1	0.7*	0.27	0.27
SrS:Tm	large (150%)	large (100%)	none	1.3	13.5	0.29	0.40
ZnS:Dy	none	none	none	1.95	11.6	0.47	0.47
SrS:Dy	none	none	yes (5%)	1.45	11.5	0.34	0.38
SrS:Dy (aged)	none	none	yes (1%)	1.4	7.7	0.43	0.44
ZnS:Ho	none	none	none	1.9	4.4	0.31	0.63
SrS:Ho	small (30%)	moderate (60%)	none	1.3	22.4	0.31	0.43
ZnS:Er	none	moderate (40%)	none	1.8	7.5	0.31	0.35
SrS:Er	small (15%)	large (100%)	none	1.2	35.0	0.28	0.58

FIGURE CAPTIONS

Figure 1. Energy band diagram illustrating the six primary physical processes responsible for ACTFEL operation. (From Ref. [9], P. D. Keir, Ph. D. Thesis, Oregon State University, 1999).

Figure 2. An L-V curve from an evaporated ZnS:Mn ACTFEL device driven by a 1 kHz bipolar trapezoidal waveform. (From Ref. [9], P. D. Keir, Ph. D. Thesis, Oregon State University, 1999).

Figure 3. An η -V curve of an evaporated ZnS:Mn ACTFEL device driven by a 1 kHz bipolar trapezoidal waveform. (From Ref. [9], P. D. Keir, Ph. D. Thesis, Oregon State University, 1999).

Figure 4. The CIE color matching functions. (From Ref. [9], P. D. Keir, Ph. D. Thesis, Oregon State University, 1999).

Figure 5. The CIE chromaticity diagram. (From Ref. [9], P. D. Keir, Ph. D. Thesis, Oregon State University, 1999).

Figure 6. Finding the dominant wavelength and color purity from CIE coordinates. (From Ref. [9], P. D. Keir, Ph. D. Thesis, Oregon State University, 1999).

Figure 7. The color gamut spanned by the colors C_1 , C_2 , and C_3 . (From Ref. [9], P. D. Keir, Ph. D. Thesis, Oregon State University, 1999).

Figure 8. PIQ/PIL measurement set up. Dashed lines denote measurement of the voltage across the sense capacitor and the voltage from the PMT. (From Ref. [75], B. A. Cleary et al., J. SID Suppl. **1**, 51, 2000, with permission from the Society for Information Display @ 2000).

Figure 9. PIL curve for evaporated ZnS:Mn ACTFEL device with a phosphor thickness of 950 nm. Filled (empty) circles correspond to the electron (hole) response. (From Ref. [75], B. A. Cleary et al., J. SID Suppl. **1**, 51, 2000, with permission from the Society for Information Display @ 2000).

Figure 10. Proposed mechanism for hole trapping-induced electron back-injection. (From Ref. [75], B. A. Cleary et al., J. SID Suppl. **1**, 51, 2000, with permission from the Society for Information Display @ 2000).

Figure 11. PIQ curve for evaporated ZnS:Mn ACTFEL device with a phosphor thickness of 950 nm. Filled (empty) circles correspond to the electron (hole) response. (From Ref. [75], B. A. Cleary et al., J. SID Suppl. **1**, 51, 2000, with permission from the Society for Information Display @ 2000).

Figure 12. PIQ for an ALE-deposited SrS:Ce ACTFEL device with a phosphor thickness of 1100 nm. (From Ref. [74], C. A. Nevers, M. S. Thesis, Oregon State University, 1999).

Figure 13. PIL for an ALE-deposited SrS:Ce ACTFEL device with a phosphor thickness of 1100 nm. (From Ref. [74], C. A. Nevers, M. S. Thesis, Oregon State University, 1999).

Figure 14. PIQ for a sputter-deposited SrS:Cu ACTFEL device with a phosphor thickness of 1100 nm. (From Ref. [74], C. A. Nevers, M. S. Thesis, Oregon State University, 1999).

Figure 15. PIL for a sputter-deposited SrS:Cu ACTFEL device with a phosphor thickness of 1100 nm. (From Ref. [74], C. A. Nevers, M. S. Thesis, Oregon State University, 1999).

Figure 16. PIQ for an MOCVD-deposited, undoped SrS ACTFEL device with a phosphor thickness of 400 nm. (From Ref. [74], C. A. Nevers, M. S. Thesis, Oregon State University, 1999).

Figure 17. Experimental apparatus for VIQ measurements. (From [76], B. A. Cleary et al., J. SID (in press), with permission from the Society for Information Display @ 2001).

Figure 18. Timing diagram for a VIQ experiment. (From [76], B. A. Cleary et al., J. SID (in press), with permission from the Society for Information Display @ 2001).

Figure 19. VIQ energy band diagram showing negative charge trapped at or near the bottom (ITO) phosphor/insulator interface. For this case, transport of photo-injected electrons generated near the bottom (ITO) interface gives rise to a positive polarity VIQ signal, as sensed from a capacitor connected to the ITO side of the ACTFEL device. (From [76], B. A. Cleary et al., J. SID (in press), with permission from the Society for Information Display @ 2001).

Figure 20. VIQ energy band diagram showing positive charge trapped at or near the bottom (ITO)

phosphor/insulator interface. In this case, transport of photo-injected holes generated near the bottom (ITO) interface gives rise to a negative polarity VIQ signal, as sensed from a capacitor connected to the ITO side of the ACTFEL device. (From [76], B. A. Cleary et al., J. SID (in press), with permission from the Society for Information Display @ 2001).

Figure 21. VIQ aging trend of an evaporated ZnS:Mn ACTFEL device. The five curves shown correspond to 0.5, 6, 30, 50, and 73 hours of aging at 1 kHz. (From [76], B. A. Cleary et al., J. SID (in press), with permission from the Society for Information Display @ 2001).

Figure 22. VIQ aging trend for an ALE (Cl) ZnS:Mn ACTFEL device. Aging is for 0, 4, and 87 hours aging at 3 kHz, with arrows indicating increasing aging time. (From [76], B. A. Cleary et al., J. SID (in press), with permission from the Society for Information Display @ 2001).

Figure 23. VIQ aging trend for an ALE (DEZ) ZnS:Mn ACTFEL device. Aging is for 0, 0.6, and 40 hours at 3 kHz, with arrows indicating increasing aging time. (From [76], B. A. Cleary et al., J. SID (in press), with permission from the Society for Information Display @ 2001).

Figure 24. Temperature-dependent VIQ for an ALE-deposited SrS:Ce ACTFEL device with a phosphor thickness of 850 nm; last applied voltage pulse is positive. Temperatures are 30, 150, 300, and 360 K. (From Ref. [74], C. A. Nevers, M. S. Thesis, Oregon State University, 1999).

Figure 25. VIQ temperature-dependent curves for a sputter-deposited SrS:Cu ACTFEL device with a phosphor thickness of 1100 nm. Temperatures are 30, 150, 300, and 360 K. (From Ref. [74], C. A. Nevers, M. S. Thesis, Oregon State University, 1999).

Figure 26. VIQ temperature-dependent curves for a MOCVD-deposited, undoped SrS ACTFEL device with a phosphor thickness of 400 nm. Temperatures are 30, 150, 300, and 360 K. (From Ref. [74], C. A. Nevers, M. S. Thesis, Oregon State University, 1999).

Figure 27. Normalized electroluminescence spectra for (a) a ZnS:Tb and (b) a SrS:Tb ACTFEL device. These spectra are obtained at a voltage of 40 V above threshold and a frequency of 1000

Hz. (Adapted from Ref. [84], P. D. Keir et al., J. Appl. Phys. **86**, 6810, 1999, with permission from the American Institute of Physics @ 1999).

Figure 28. Normalized electroluminescence spectra for (a) a ZnS:Er and (b) a SrS:Er ACTFEL device. These spectra are obtained at a voltage of 40 V above threshold and a frequency of 1000 Hz. (From Ref. [84], P. D. Keir et al., J. Appl. Phys. **86**, 6810, 1999, with permission from the American Institute of Physics @ 1999).

Figure 29. Normalized electroluminescence spectra for (a) a ZnS:Ho, (b) a SrS:Ho ACTFEL device, (c) a BaS:Ho ACTFEL device, (d) a CaS:Ho ACTFEL device, and (e) a CaSe:Ho ACTFEL device. These spectra are obtained at a voltage of 40 V above threshold and a frequency of 1000 Hz. (Adapted from Ref. [84], P. D. Keir et al., J. Appl. Phys. **86**, 6810, 1999, with permission from the American Institute of Physics @ 1999, and from Ref. [85], C. M. Maddix, M. S. Thesis, Oregon State University, 2000).

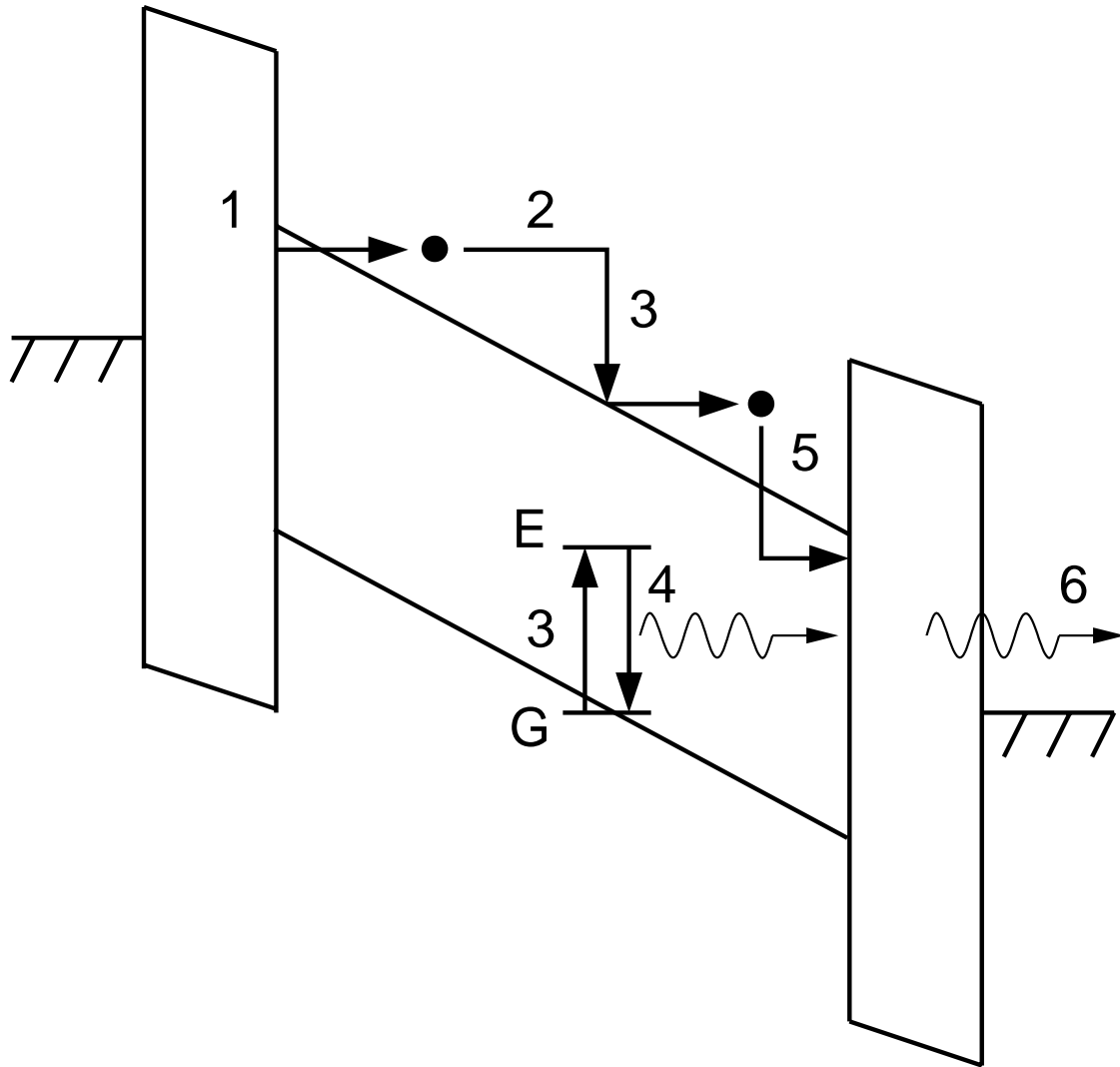


Figure 1: baukol et al.

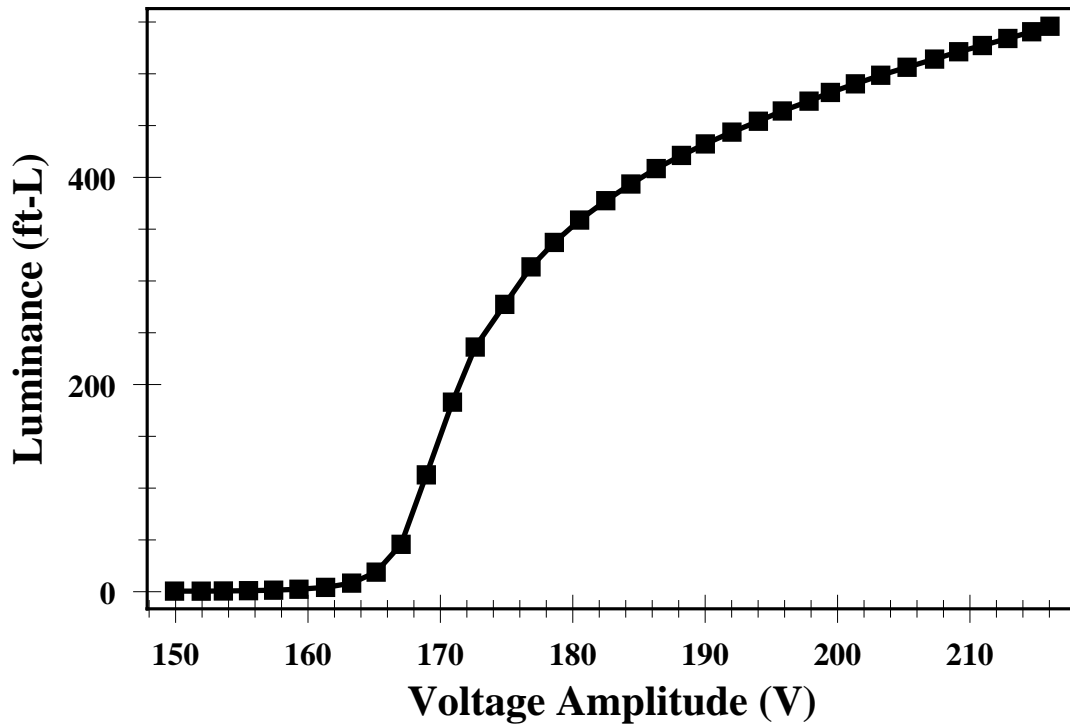


Figure 2: baukol et al.

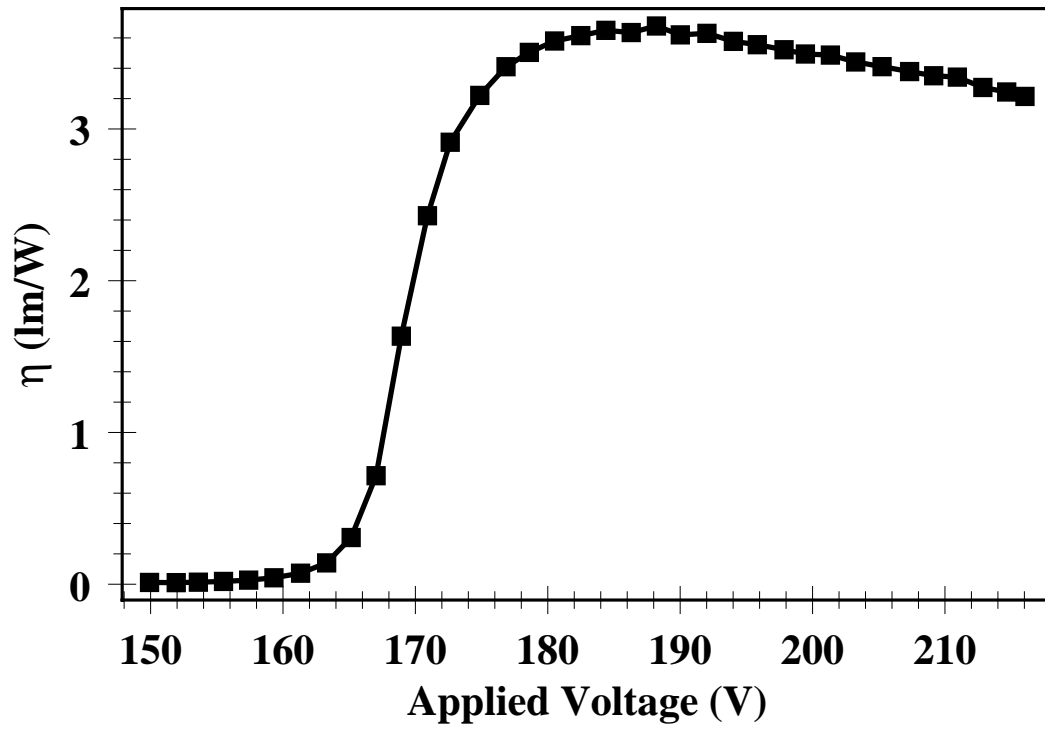


Figure 3: baukol et al.

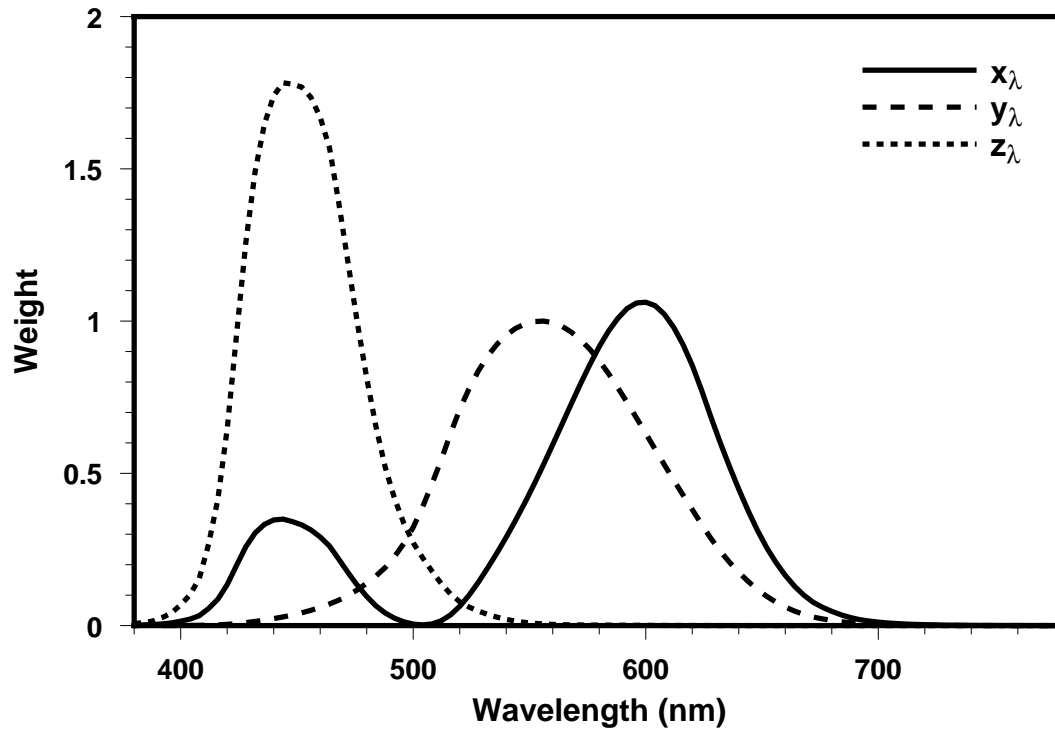


Figure 4: baukol et al.

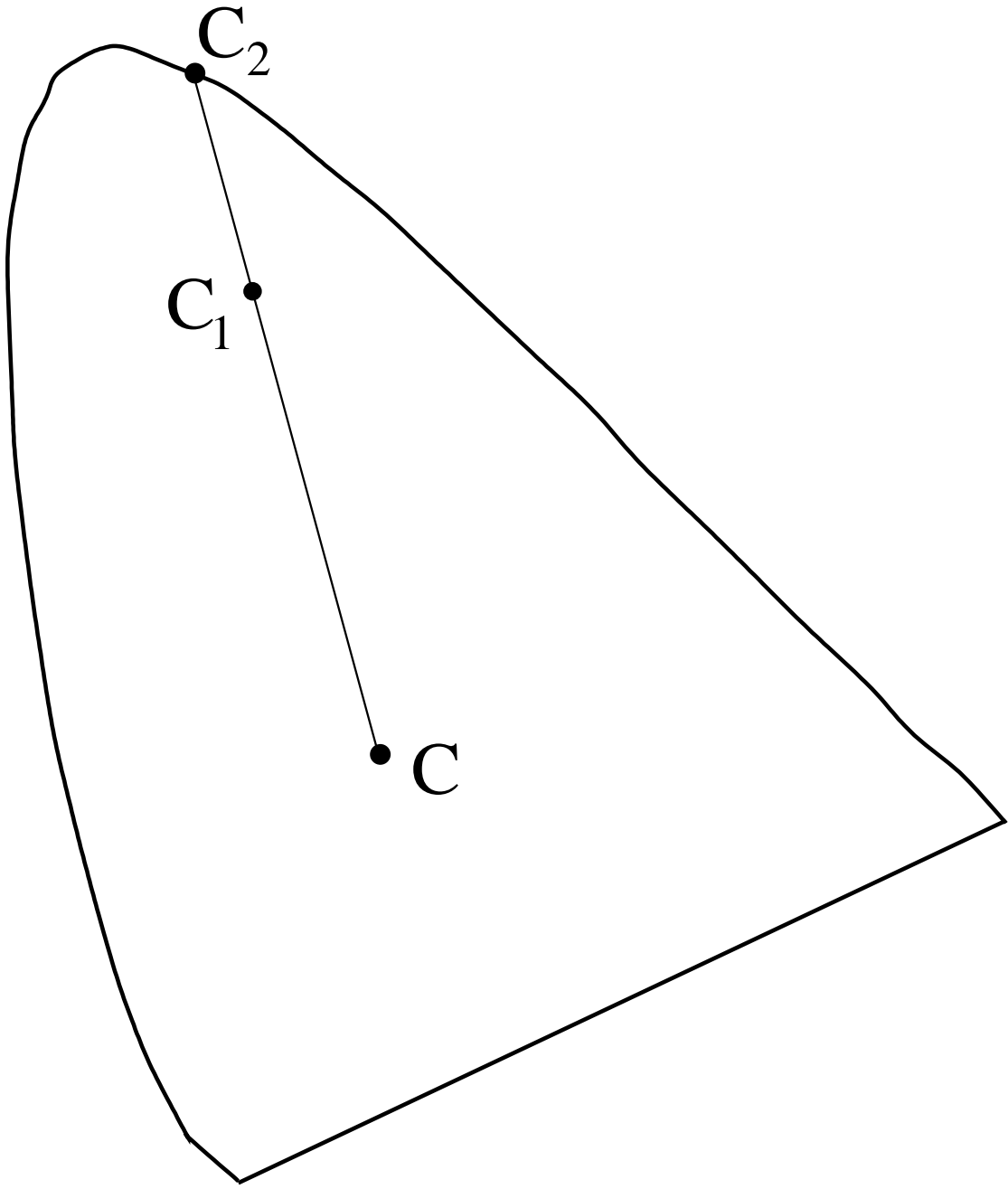


Figure 6: baukol et al.

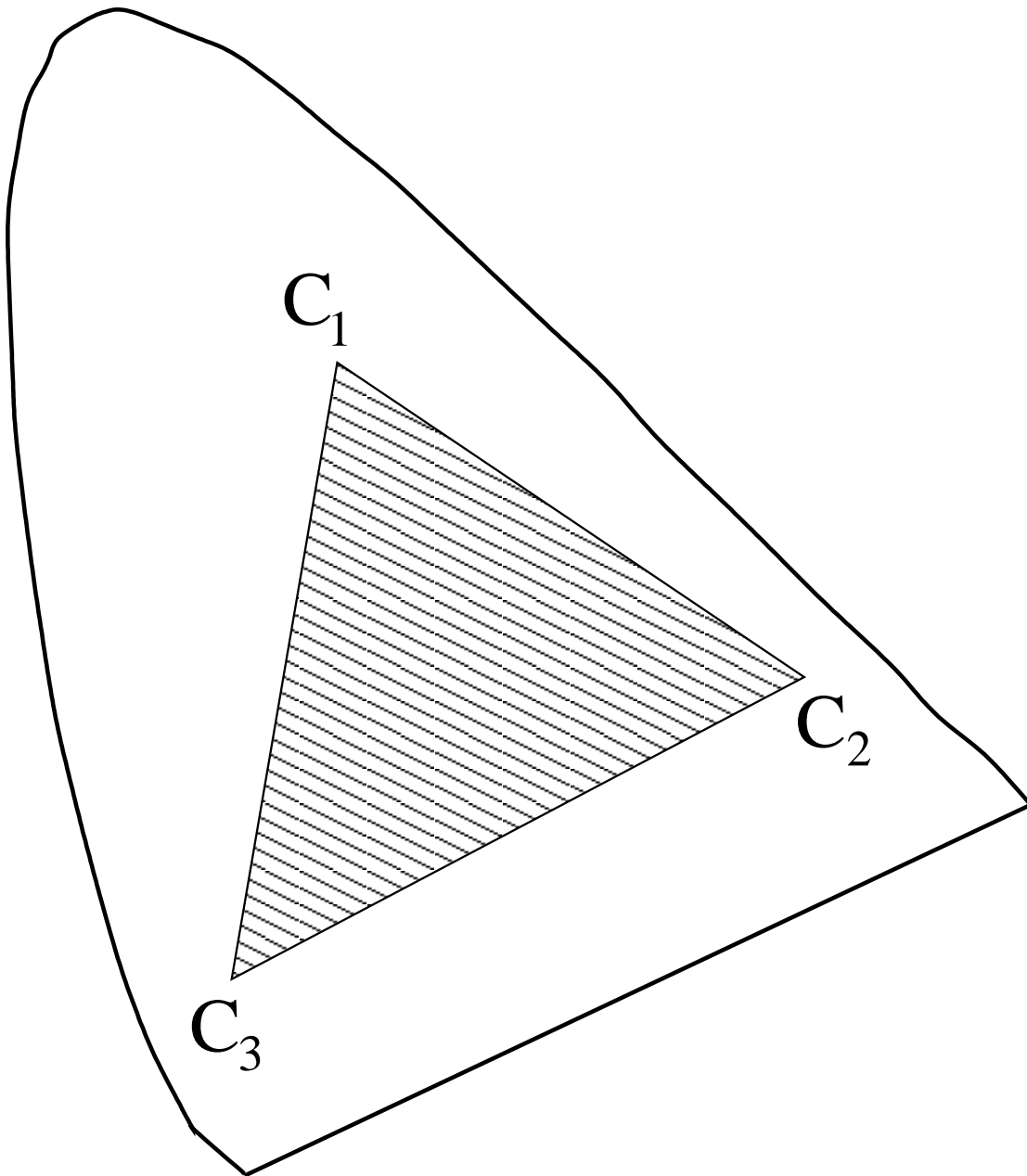


Figure 7: baukol et al.

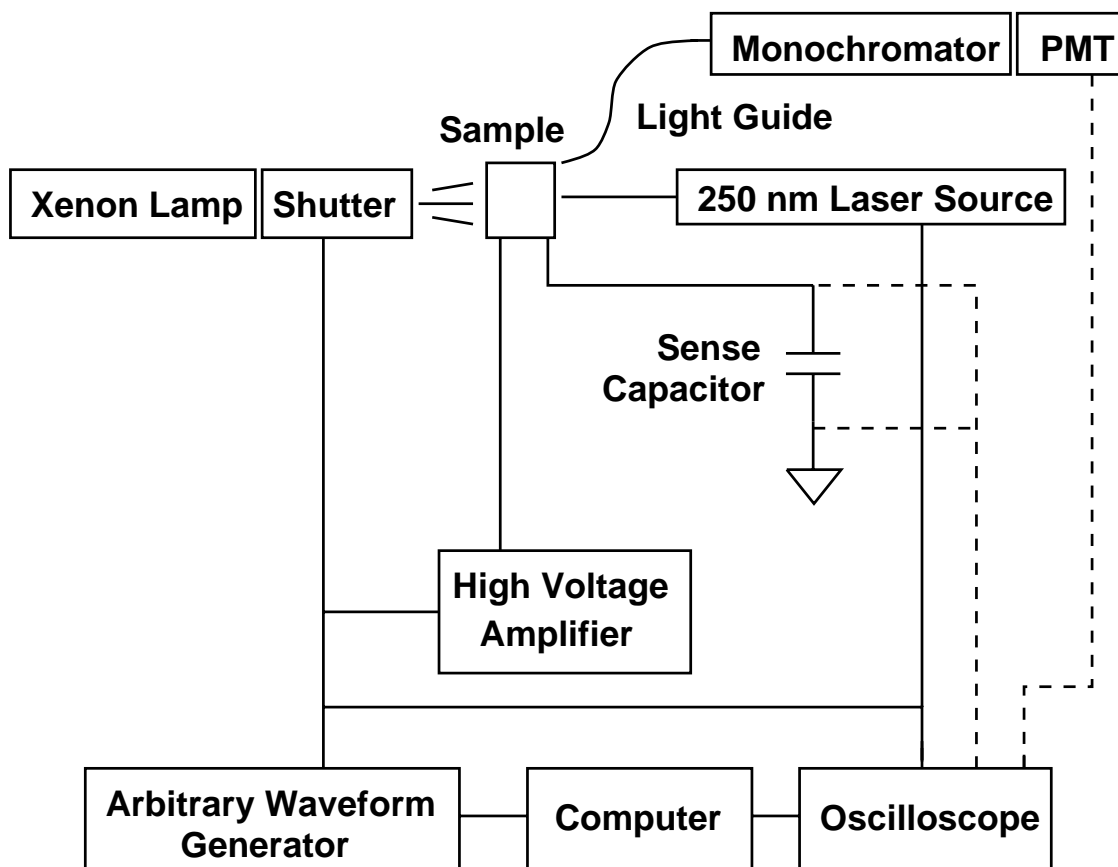


Figure 8: baukol et al.

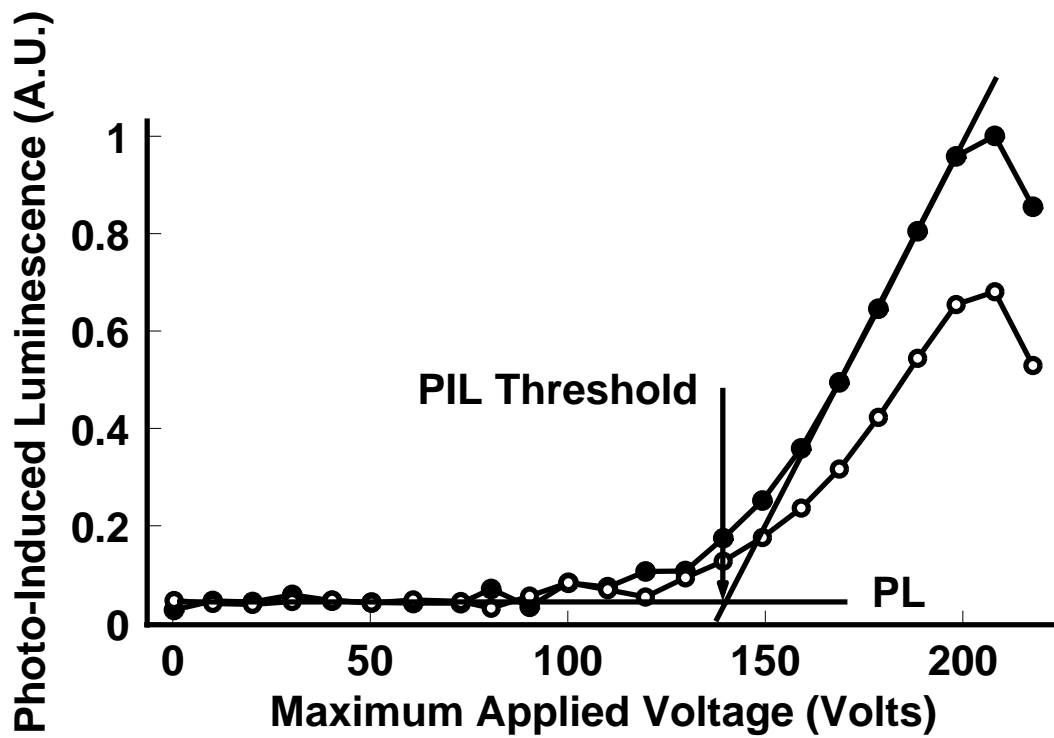


Figure 9: baukol et al.

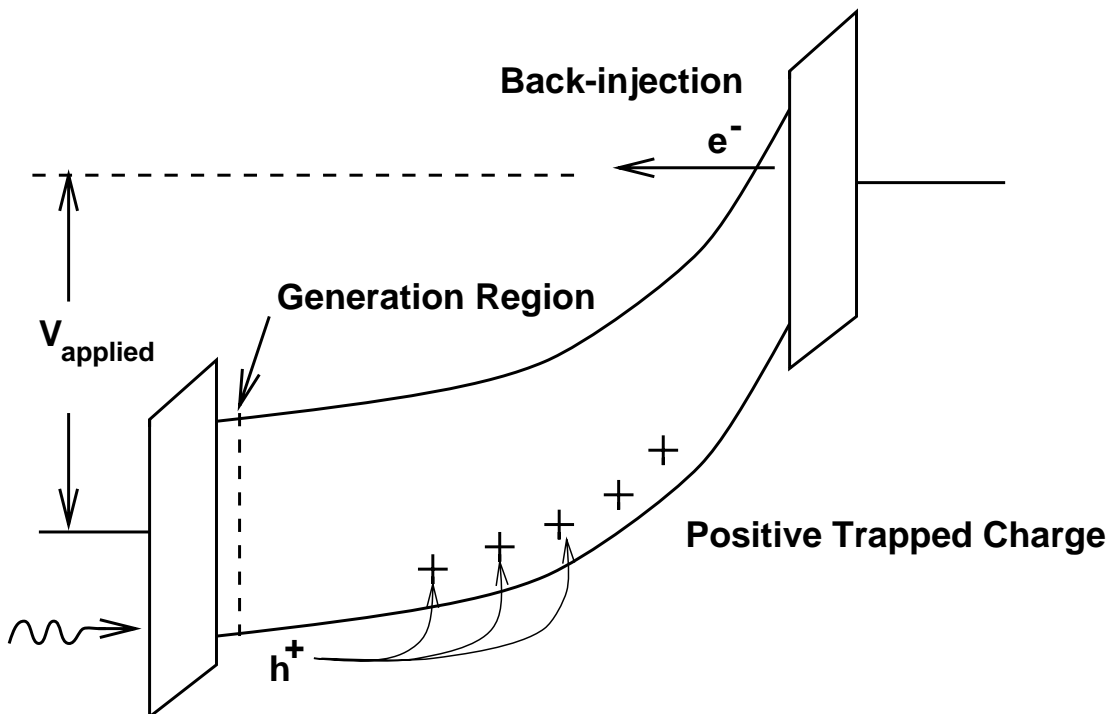


Figure 10: baukol et al.

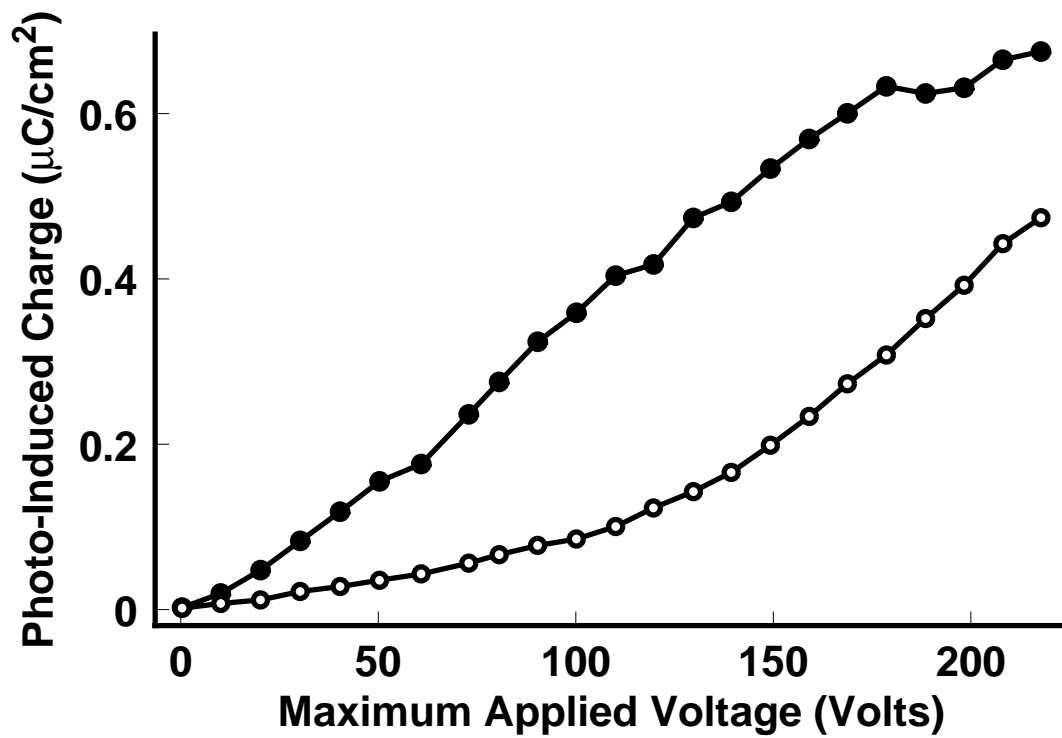


Figure 11: baukol et al.

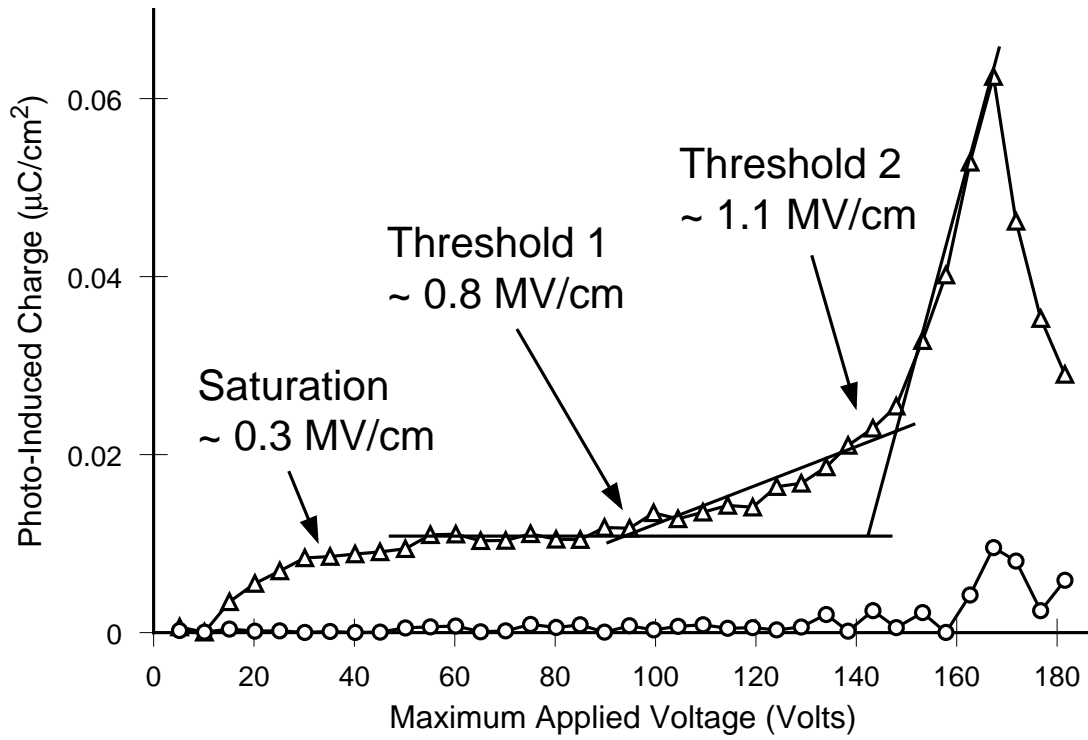


Figure 12: baukol et al.

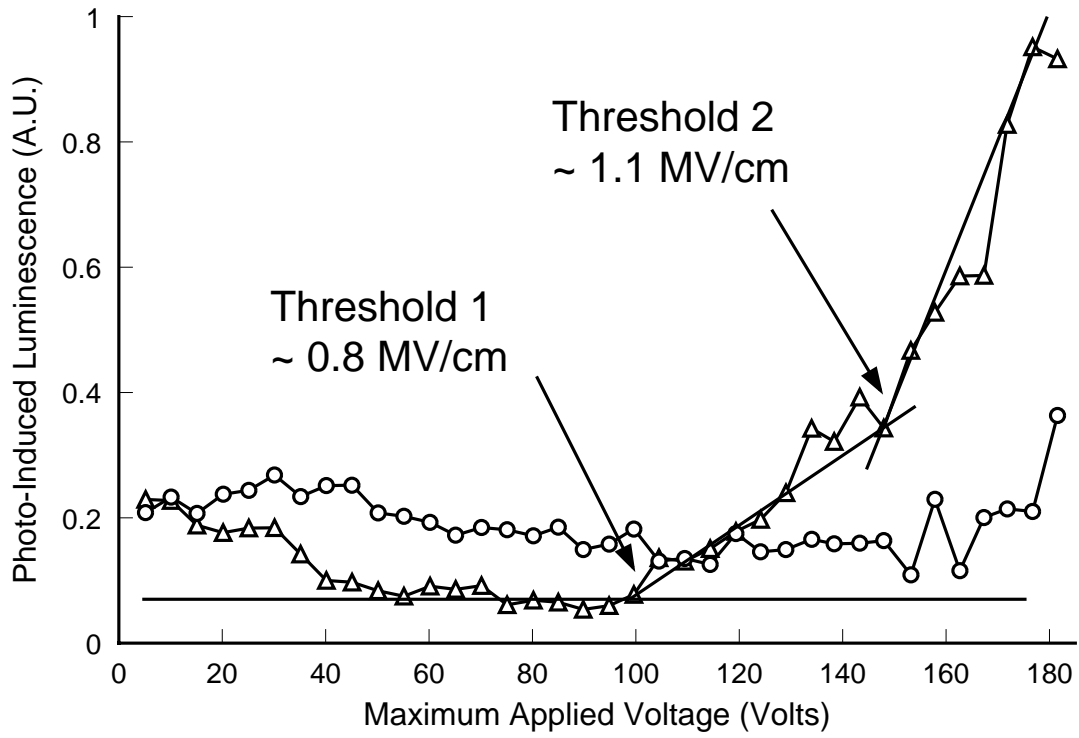


Figure 13: baukol et al.

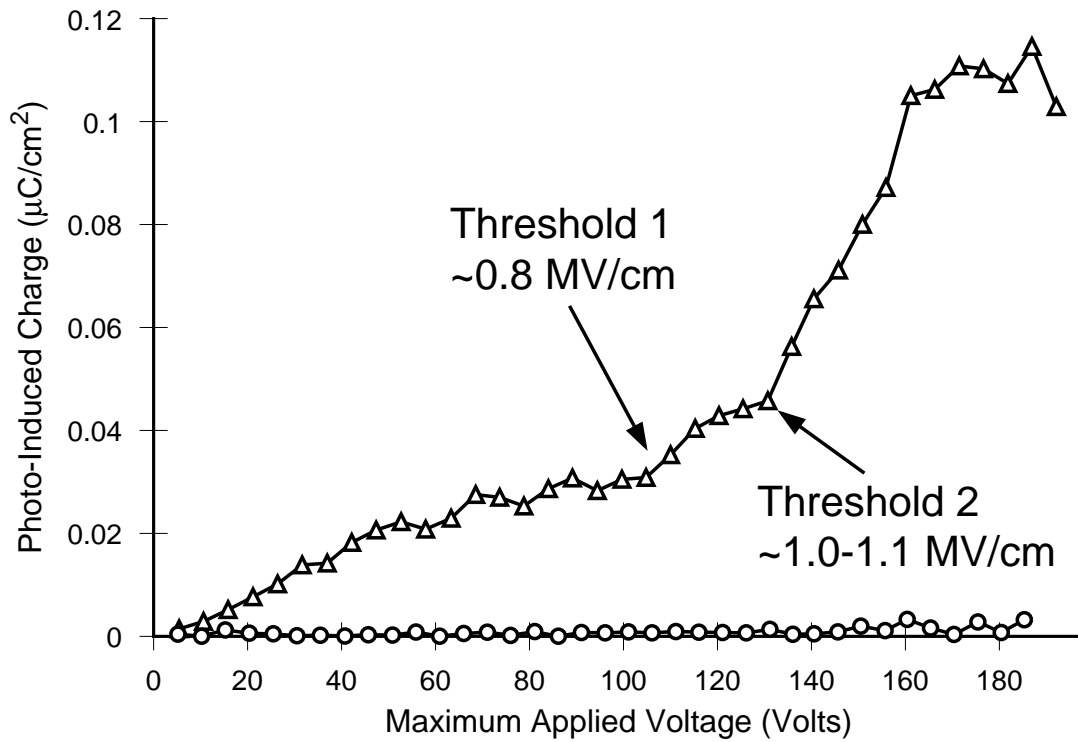


Figure 14: baukol et al.

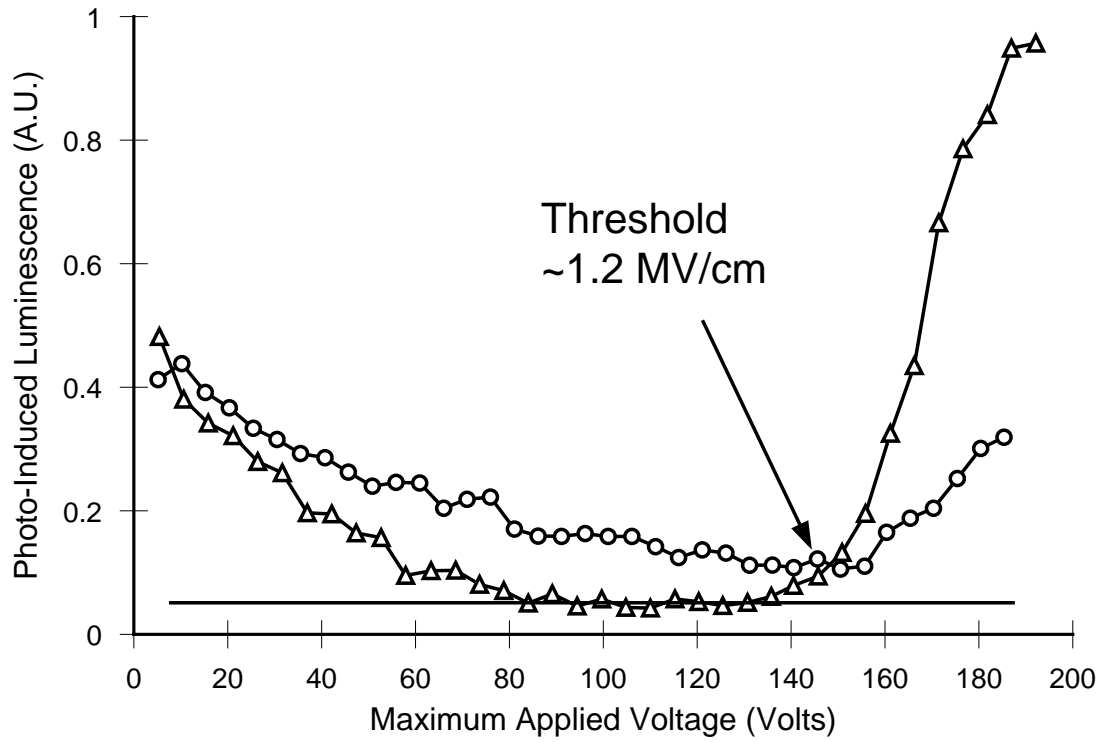


Figure 15: baukol et al.

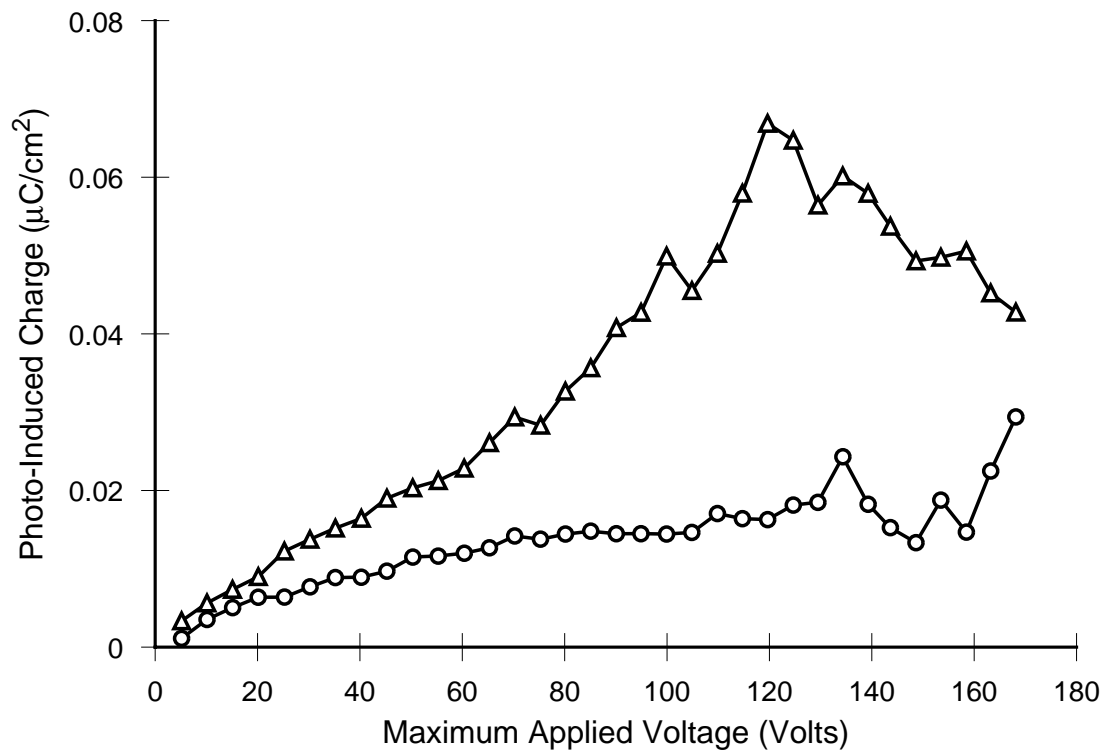


Figure 16: baukol et al.

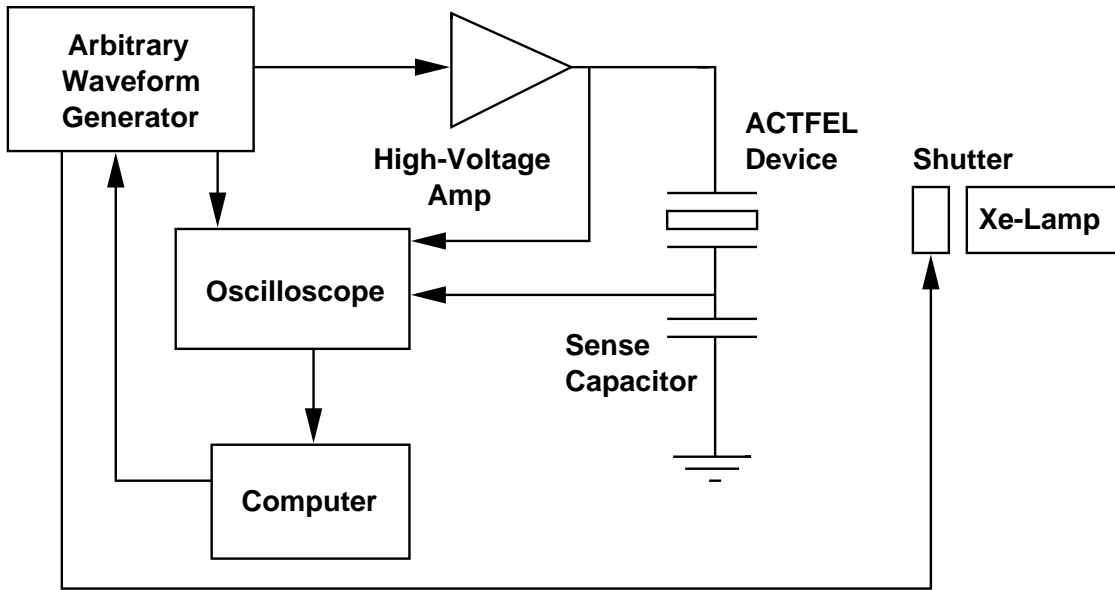


Figure 17: baukol et al.

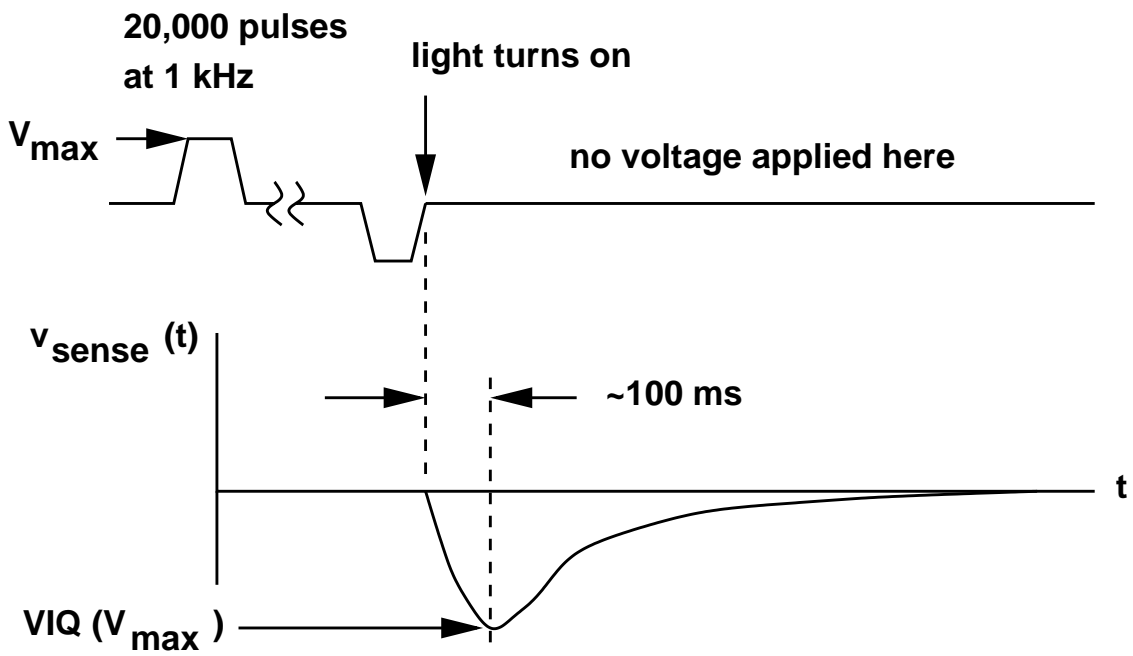


Figure 18: baukol et al.

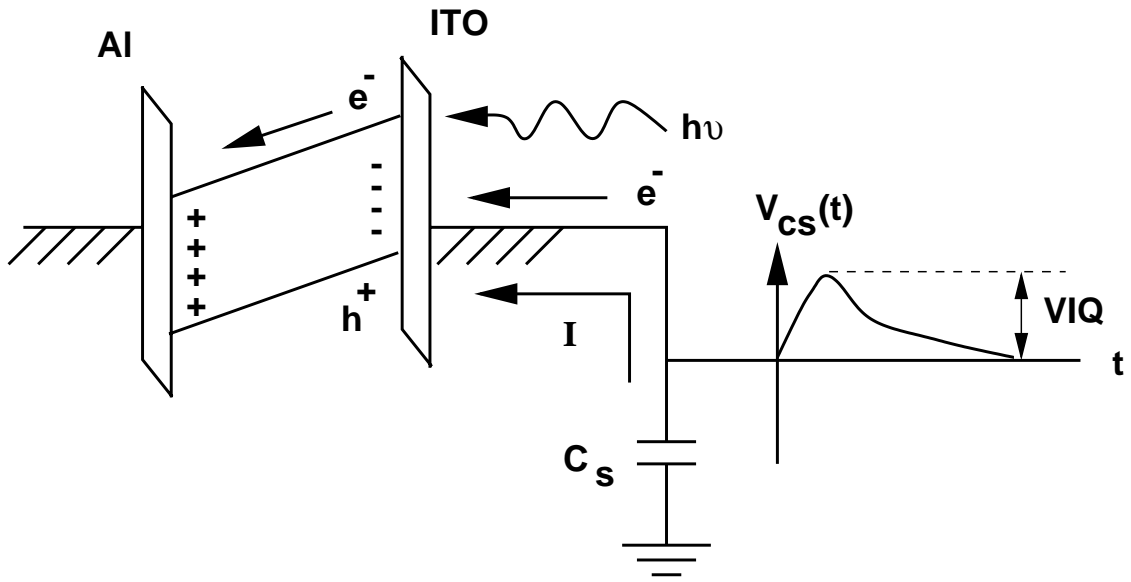


Figure 19: baukol et al.

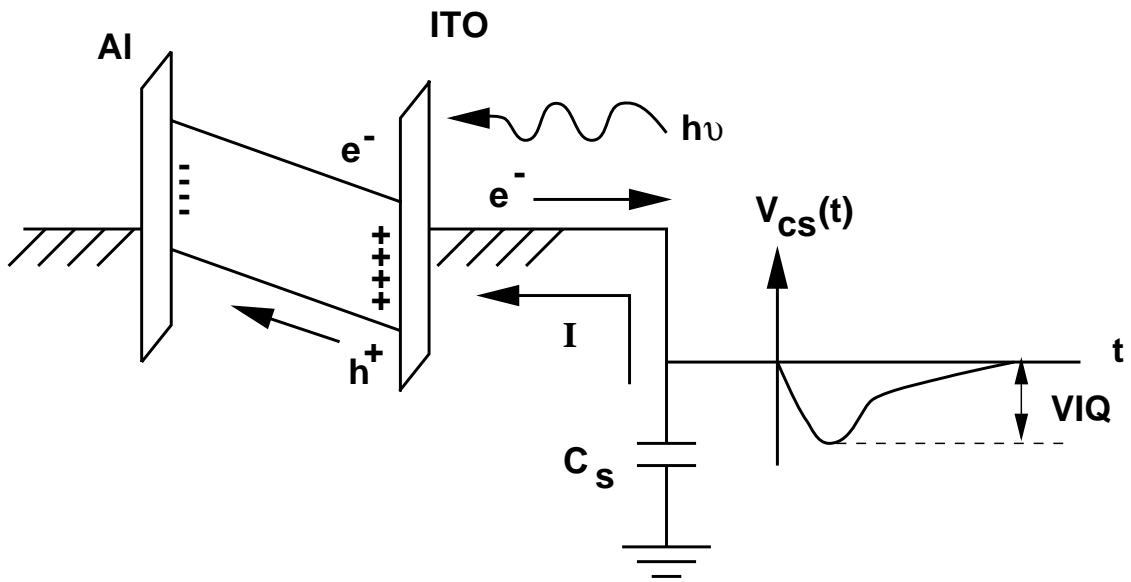


Figure 20: baukol et al.

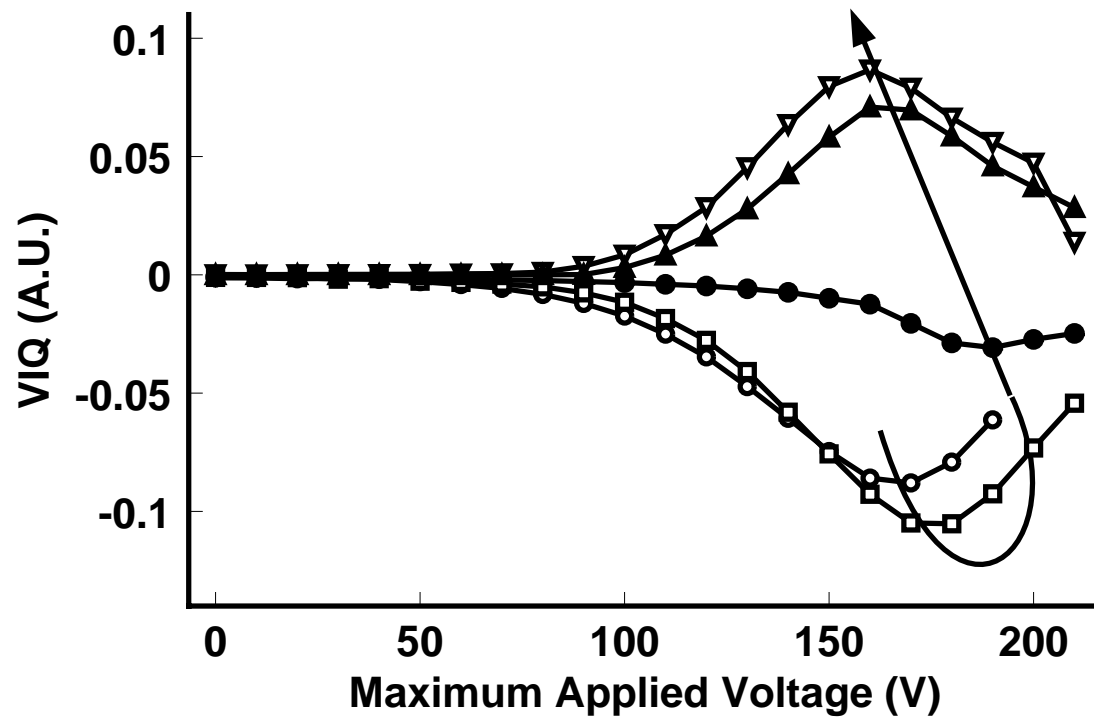


Figure 21: baukol et al.

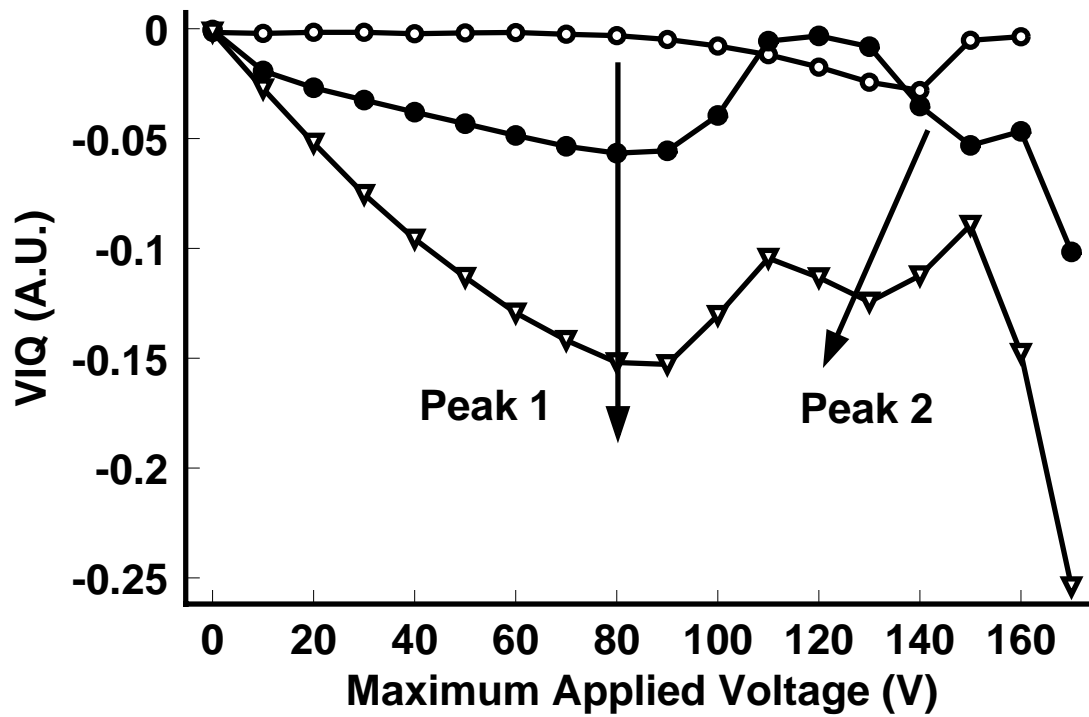


Figure 22: baukol et al.

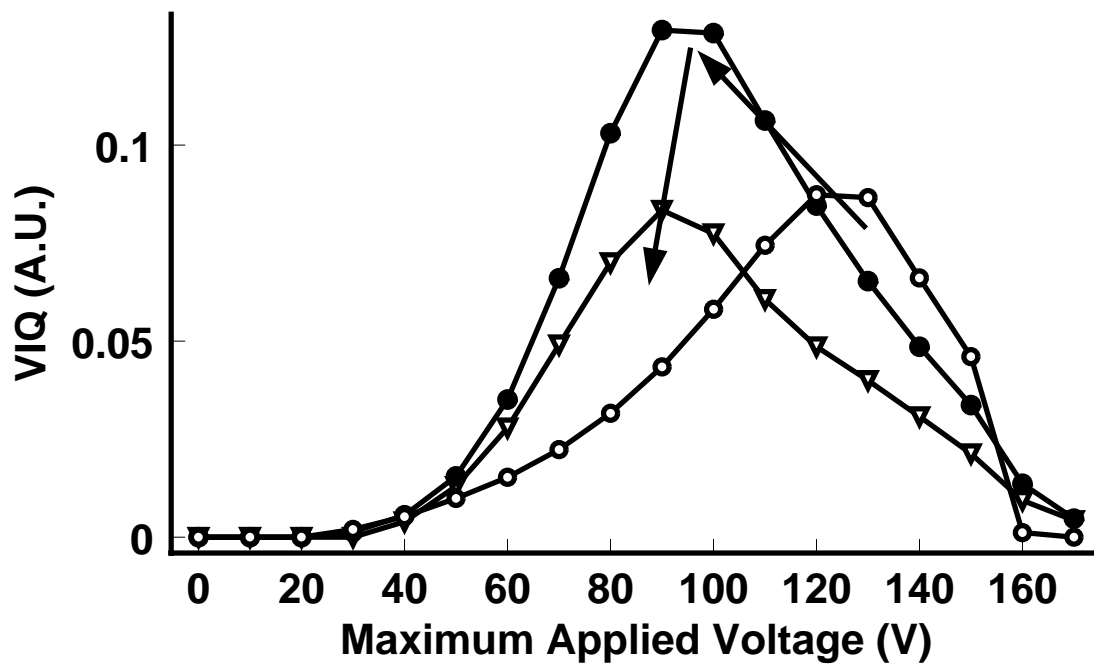


Figure 23: baukol et al.

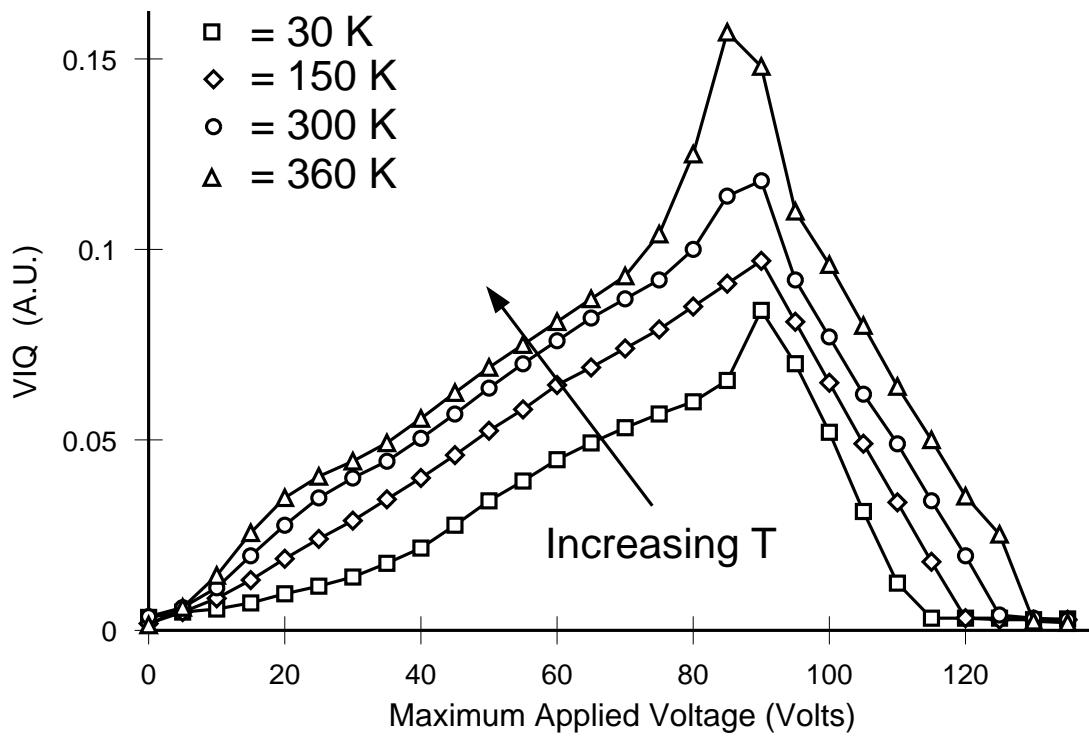


Figure 24: baukol et al.

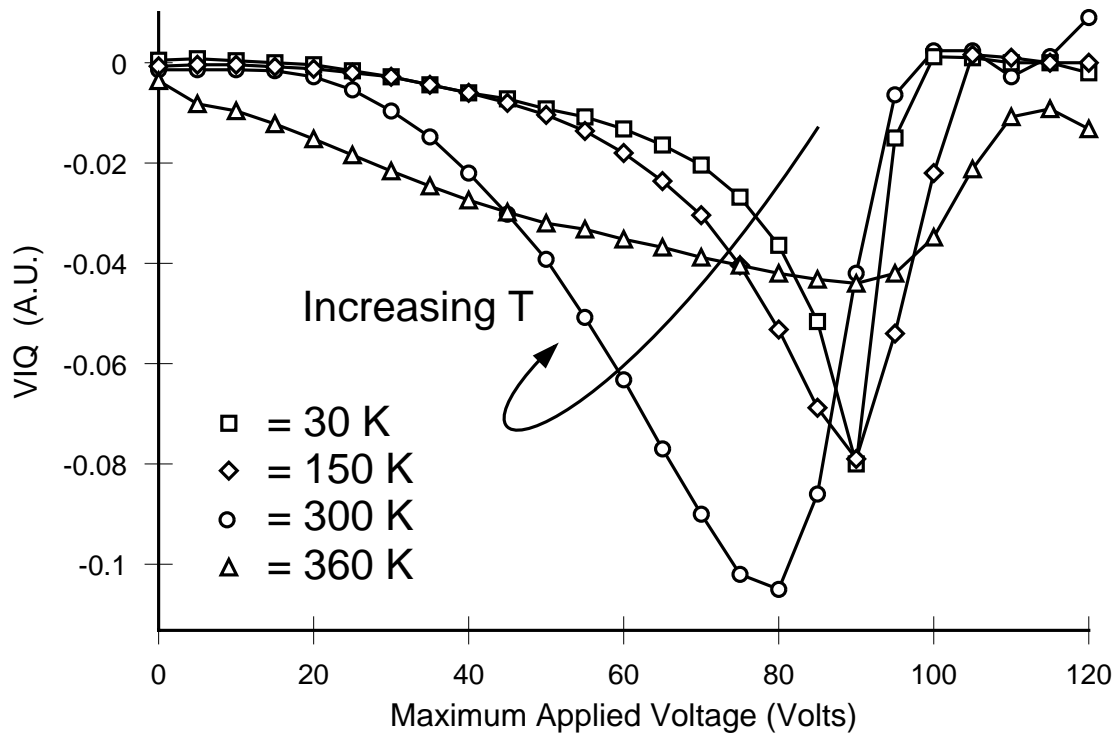


Figure 25: baukol et al.

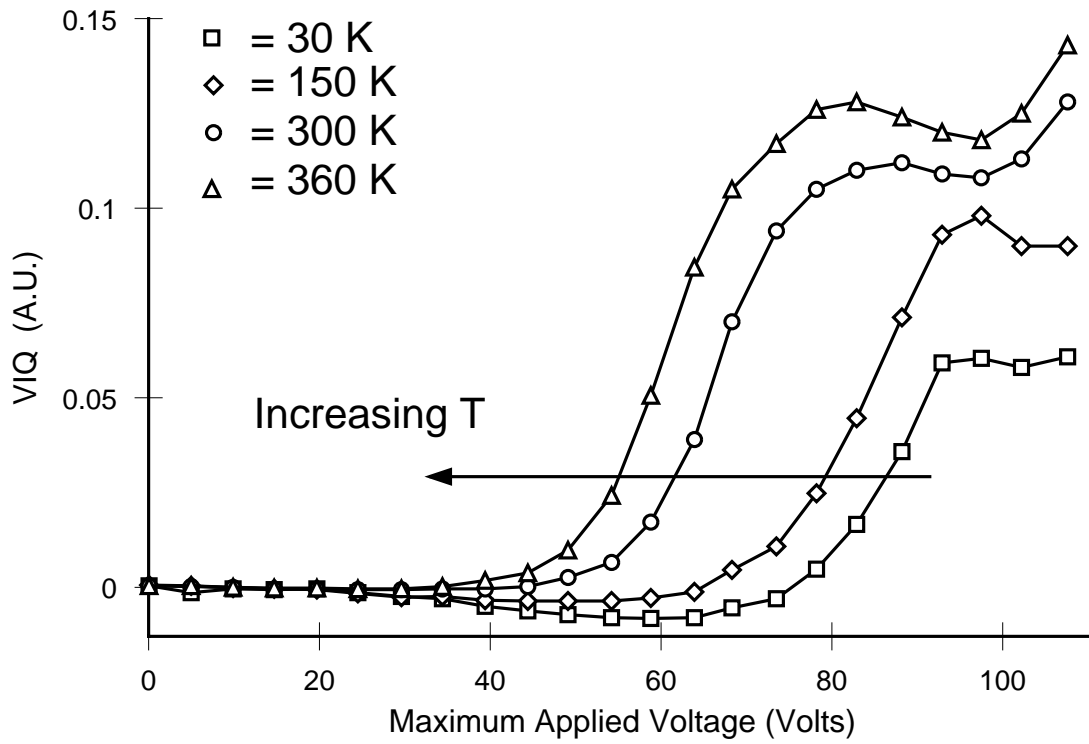


Figure 26: baukol et al.

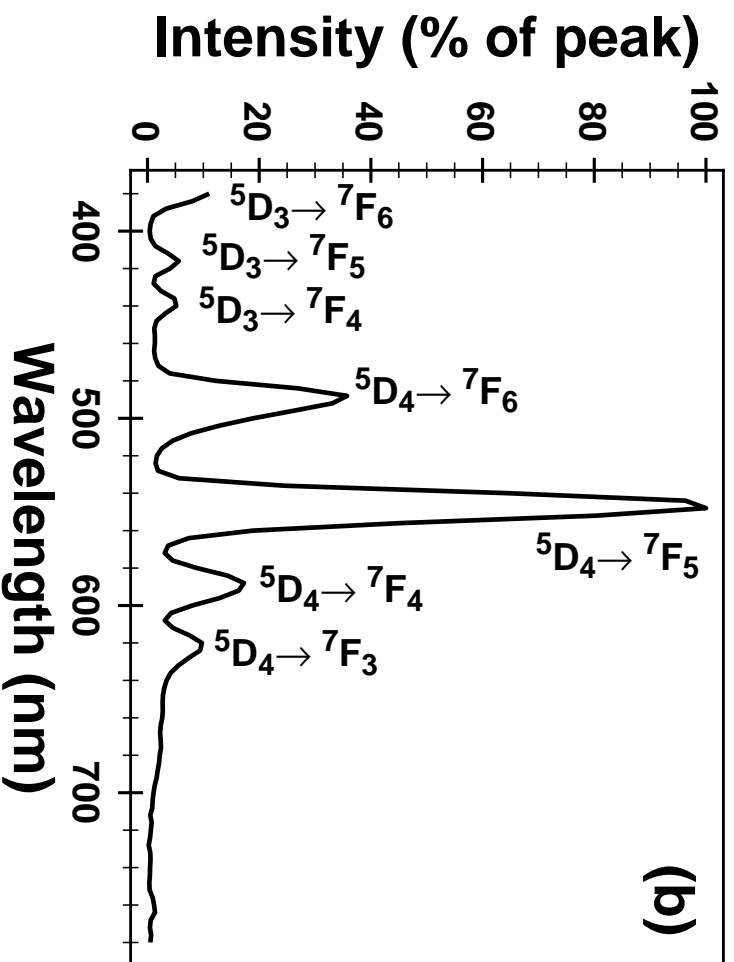
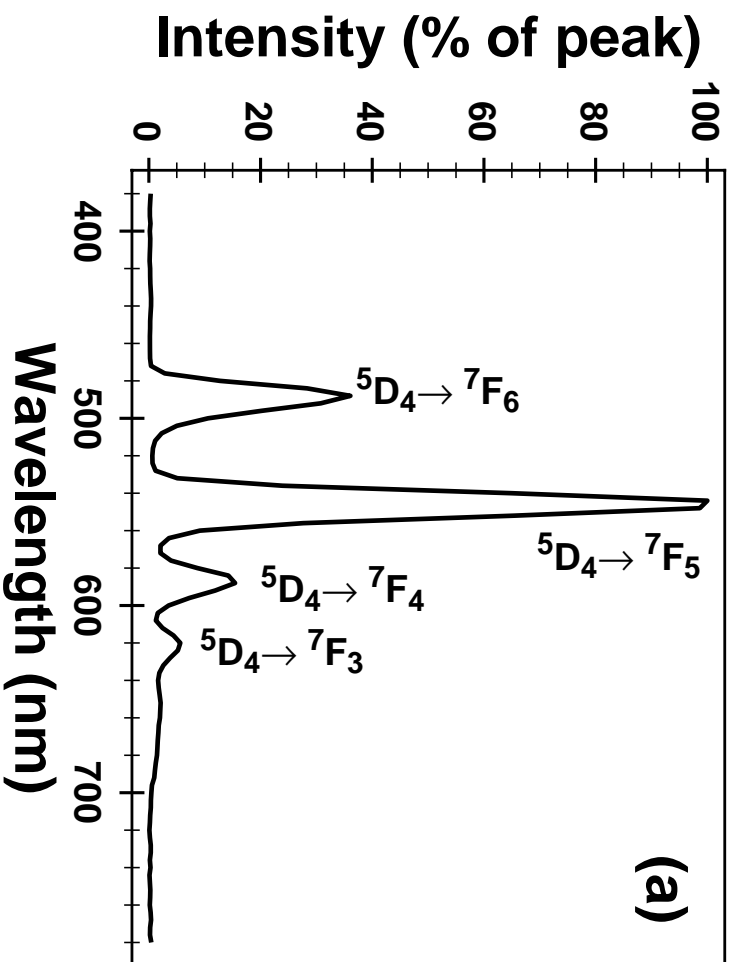


Figure 27: baukol et al.

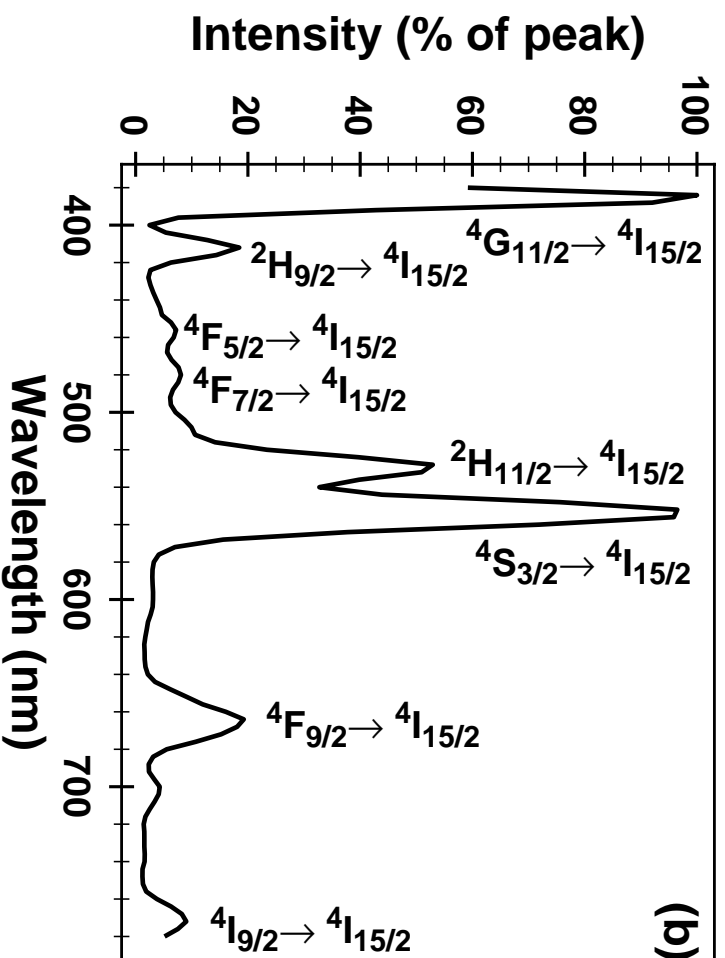
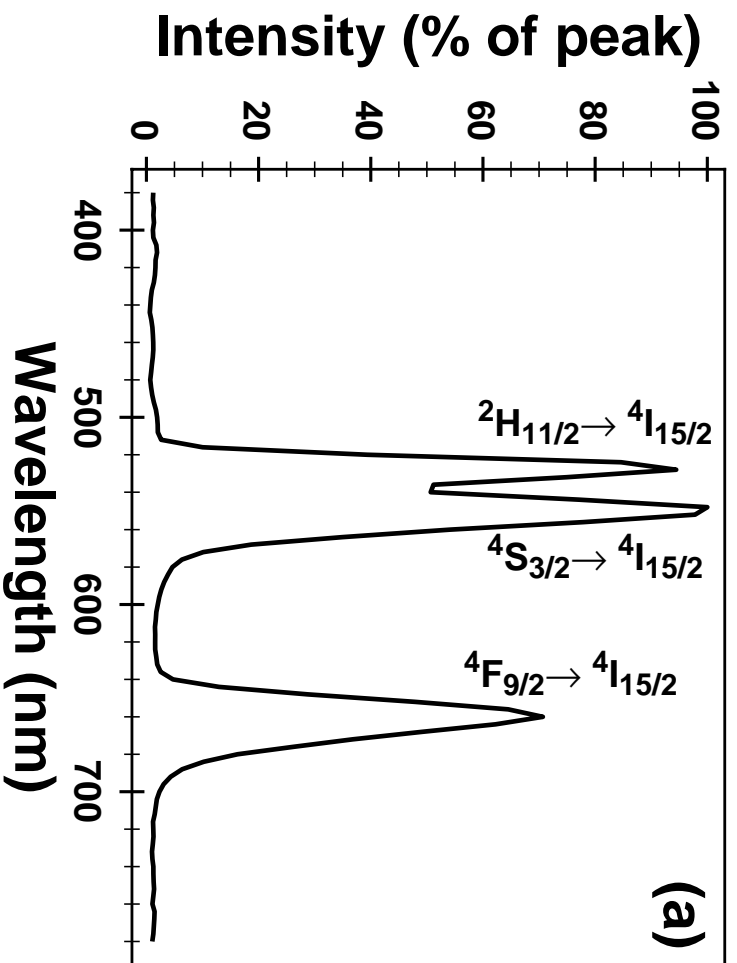


Figure 28: baukol et al.

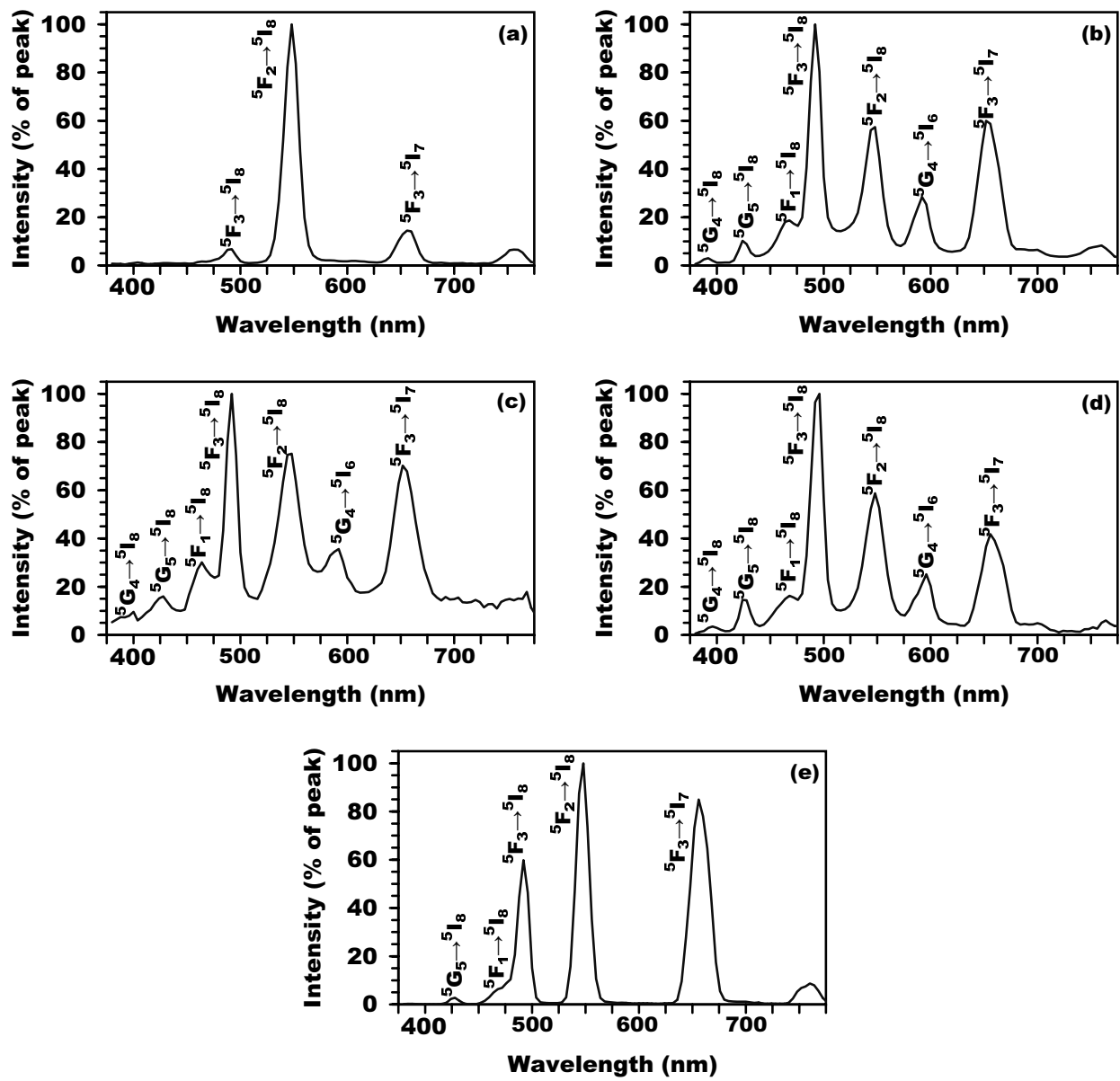


Figure 29: baukol et al.